POLITECNICO DI TORINO

Collegio di Ingegneria Chimica e dei Materiali

Master of Science Course
in Materials Engineering for Industry 4.0

Master of Science Thesis

Development and characterization of borate-modified $Li_{1.5}Al_{0.3}Mg_{0,1}Ge_{1.6}(PO_4)_3$ NASICON-type electrolytes

Supervisor/s

Prof. Claudio Gerbaldi
Prof. Federico Smeacetto

Candidate

Lorenzo Primo

October 2025

Abstract

As the world transitions to renewable electricity and electrifies more of its energy demand, power generation and use are being transformed, with batteries taking center stage. They are already indispensable in portable electronics and have become the key enabling technology for electric vehicles, where very high energy density is critical. However, conventional lithium-ion batteries are constrained by important drawbacks: the flammability of liquid electrolytes, the limited energy density, and the reliance on scarce raw materials.

Solid-state batteries have emerged as suitable alternative for next-generation devices, aiming to overcome these challenges by replacing the liquid electrolyte with a solid-state one, either inorganic, polymeric or composite/hybrid. This architecture promises enhanced safety, compatibility with metallic lithium or sodium anodes, suppression of dendrite growth and potentially, higher energy density. Yet, solid-state batteries still face major hurdles, including insufficient room-temperature conductivity, unstable electrode–electrolyte interfaces, and reduced electrochemical performance due to poor solid–solid contact. Progress in this field critically depends on the discovery and optimization of advanced solid electrolytes, with NASICON-type glass-ceramics among the most promising candidates.

In such scenario, this Master's Degree Thesis addresses these challenges by investigating the influence of borate modifiers on the $Li_{1.5}Al_{0.3}Mg_{0.1}Ge_{1.6}(PO_4)_3$ (LAMGP), a promising NASICON-type glass-ceramic solid electrolyte material. To establish the scientific context, the state of the art of ceramic electrolytes is first reviewed, focusing on the main structural families, discussing their conduction mechanisms, processing strategies, practical limitations and the effect of doping elements. In particular, the addition of B_2O_3 has been shown to significantly improve the properties of this system. On this foundation, the work proceeds with an experimental study of LAMGP glass-ceramics modified with $LiBO_2$ and $Li_2B_4O_7$, with the aim of achieving effects comparable to B_2O_3, analyzing how these additives affect crystallization behavior, microstructure, and electrochemical properties. This approach allows for a systematic correlation between composition, microstructure, and performance, with the goal of identifying how borate additives can be exploited to optimize NASICON-type electrolytes for solid-state battery applications.

Results demonstrate that the addition of borate phases significantly affects the crystallization pathway and microstructure of the glass-ceramics. $LiBO_2$ promotes the formation of cohesive crystallites, enhancing densification and leading to improved ionic conductivity. Conversely, $Li_2B_4O_7$ tends to favor the development of secondary phases, resulting in microstructural heterogeneities and poorer conductivity response.

Overall, the study confirms that the careful selection and tuning of glass modifiers in LAMGP systems can tailor the balance between densification, crystallization, and ionic conductivity. The findings contribute to a deeper understanding of structure–property correlations in borate-modified NASICON-type glass-ceramic electrolytes, highlighting their potential and paving the way for safer and more efficient lithium-based solid-state batteries.

Table of Contents

Chapter 1

Introduction

The transition to a sustainable energy economy is one of the major technological challenges of the 21st century. Climate change, driven largely by greenhouse gas emissions from fossil fuel combustion, requires the rapid adoption of renewable energy sources and efficient means of storing intermittent electricity generated from solar and wind power. At the same time, the demand for electrified transportation and portable electronics continues to rise, pushing the limits of current energy storage technologies. In this context, batteries have emerged as indispensable devices, capable of combining high energy density with versatility of design.

A battery is an electrochemical power source that stores energy in chemical form and releases it through red-ox reactions. A schematic representation of a Li-ion electrochemical cell in discharge is shown in Figure 1.1.

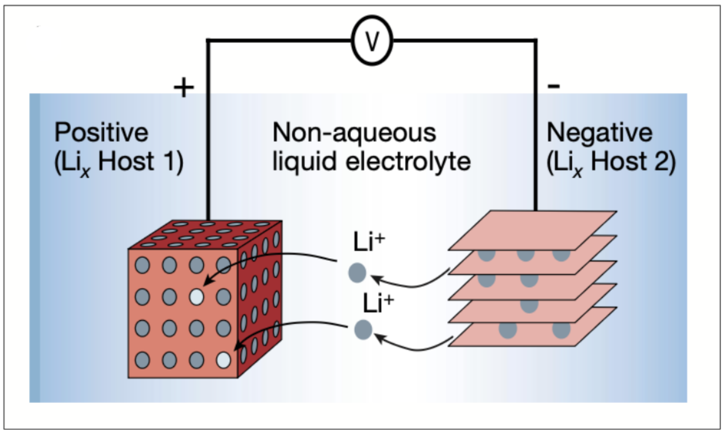

Figure 1.1: Schematic representation of a rechargeable lithium-ion cell in discharge. Source: [1].

Each cell consists of a positive and a negative electrode separated by an electrolyte that enables ionic transport between them. During discharge, the anode undergoes oxidation, releasing electrons to the external circuit, while the cathode undergoes reduction, accepting electrons. The voltage of the cell is governed by the difference in chemical potential between the electrodes, limited by the stability window of the electrolyte. A distinction is made between primary batteries, which undergo an irreversible discharge reaction, and secondary batteries, where an external current can reverse the electron flow and drive the non-spontaneous reaction, restoring the electrodes to their charged state [2]. Over the past decades, different chemistries have been developed to embody the second one, ranging from lead–acid and nickel-based systems to the lithium-ion technologies that now dominate portable applications.

Although remarkable progress has been achieved in other technological fields, the development of energy storage has often been regarded as comparatively slow. Legacy systems such as nickel–cadmium and nickel–metal hydride enabled the first generation of portable applications, but were soon overtaken by lithium-based technologies thanks to their higher energy density [1]. Energy densities of different systems is reported in Figure 1.2.

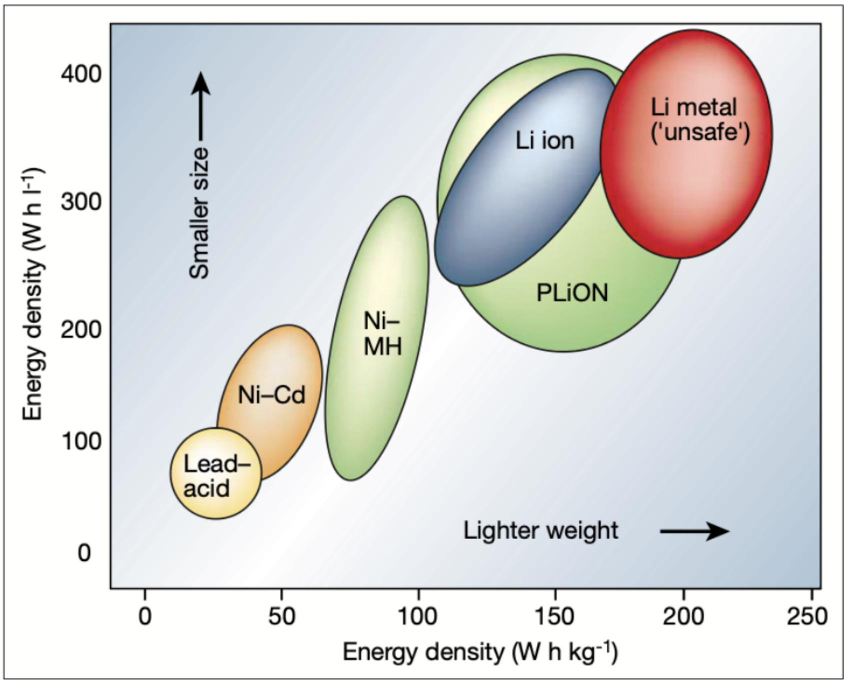

Figure 1.2: Comparison of the different battery technologies in terms of volumetric and gravimetric energy density. Source: [1].

The search for high-energy batteries naturally turned to lithium, the lightest and most electropositive metal, offering unmatched energy density. Primary lithium cells introduced in the 1970s rapidly found use in small electronics, but attempts at rechargeable systems with metallic lithium soon faced safety issues caused by dendritic growth during cycling, of which the process is shown in Figure 1.3. Progress came with the discovery of intercalation compounds, which allowed lithium to be reversibly stored within layered hosts. Early work on TiS_2 cathodes laid the foundation, but it was the combination of $LiCoO_2$ cathodes with carbon anodes that enabled the breakthrough. In 1991, Sony commercialized the first lithium-ion cell, delivering roughly 3.6 V, transforming portable electronics and establishing the technology as the market leader [1].

Three decades after their commercialization, lithium-ion batteries are a consolidated technology powering most portable electronics and increasingly dominating electric vehicles and grid storage. Their success stems from continuous improvements in electrode chemistry and cell design. $LiCoO_2$, the first commercial cathode, remains in use but has been progressively complemented by Ni- and Mn-rich layered oxides, which offer higher capacities and reduced cobalt dependence. Spinel structures such as $LiMn_2O_4$ provide cost and safety advantages, while polyanion compounds, notably $LiFePO_4$, deliver excellent thermal stability at lower cost. On the anode side, carbon remains the standard, though alloying and conversion materials are under development to increase capacity. Despite these advances, challenges persist in reconciling high energy density with safety, sustainability, and cost, which continues to drive research into both improved chemistries and next-generation concepts [3].

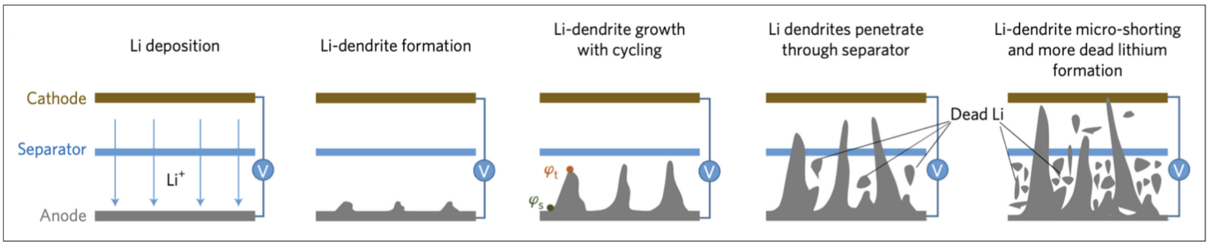

Figure 1.3: Dendrite formation and growth in Li-ion cells that eventually leads to cell shortcut and failure. Adapted from: [4].

Despite the remarkable success of lithium-ion technology, further progress is constrained by intrinsic limitations of liquid electrolytes, including safety risks, limited electrochemical stability, and difficulties in achieving higher energy densities. These challenges have accelerated the search for next-generation systems where the liquid electrolyte is replaced by a solid counterpart. Solid-state batteries offer the prospect of improved safety, longer cycle life, and the possibility of employing high-capacity lithium metal anodes, making them one of the most promising directions for future energy storage research.

In parallel to the development of lithium technology, a more recent branch of research has focused on sodium batteries. The main driver is the need to diversify raw material supply chains and reduce reliance on lithium, which is relatively scarce, unevenly distributed, and increasingly costly. Sodium, by contrast, is the sixth most abundant element in the Earth's crust, widely available at low cost, and shares similar electrochemistry with lithium. These attributes make it highly attractive for large-scale, low-cost applications where sustainability and resource accessibility are as important as performance [5].

The working principle of sodium-ion batteries is analogous to that of lithium-ion cells: sodium ions shuttle between positive and negative electrodes through an electrolyte during charge and discharge. Cathodes are typically Prussian Blue Analogs or polyanionic materials like NVPF ($Na_3V_2(PO_4)_2F_3$), while anodes are most often disordered carbons (hard carbon), since graphite cannot effectively intercalate sodium under ambient conditions. However, because of sodium's larger ionic radius, the achievable energy density is lower than that of lithium-ion batteries [6, 7].

At present, sodium-ion batteries remain a technology in development. While several companies have demonstrated prototypes and even pilot-scale production, widespread commercialization has not yet occurred. Their strategic role is therefore not to replace lithium-ion batteries in portable electronics or high-performance electric vehicles, but to complement them in applications where cost, abundance, and scalability are more critical than maximum energy density, such as stationary grid storage, power tools and city cars. Table 1.1 shows the differences between the two technologies, highlighting their complementary role.

Table 1.1: Comparison of lithium-ion and sodium-ion batteries (approximate values from recent literature [5]).

Property	**Lithium-ion**	**Sodium-ion**
Gravimetric energy density	150–250 Wh kg^{-1}	100–160 Wh kg^{-1}
Volumetric energy density	400–700 Wh L^{-1}	200–400 Wh L^{-1}
Typical anode	Graphite	Hard carbon
Critical raw material required	Li, Co, Ni	Transition metals
Approximate cell cost (2023 est.)	120–150 USD kWh^{-1}	Potentially $<$ 100 USD kWh^{-1}
Commercial status	Mass-produced	Early development

This work focuses on to the investigation of the latest developments in solid-state batteries, in particular on ceramic electrolytes for Lithium systems. These materials are at the front of current research due to their wide electrochemical stability and mechanical robustness, which together address many of the safety and performance limitations of liquid electrolytes. By exploring recent strategies for improving ceramic electrolytes, this thesis aims to contribute to the advancement of solid-state battery technologies as next-generation energy storage solutions.

Chapter 2

Solid state batteries

2.1 Working principles and comparison with standard Li-ion batteries

Solid-state batteries (SSBs) are attracting increasing attention as a next-generation energy storage technology. Their defining feature is the replacement of flammable organic liquid electrolytes with solid ionic conductors, a change that fundamentally alters both safety and performance. The elimination of volatile solvents addresses the risks of leakage, combustion, and thermal runaway that remain critical limitations of conventional lithium-ion batteries, especially in large-scale applications such as electric vehicles and stationary storage [8]. Figure 2.1 gives a visual representation of the main advantages of this kind of batteries.

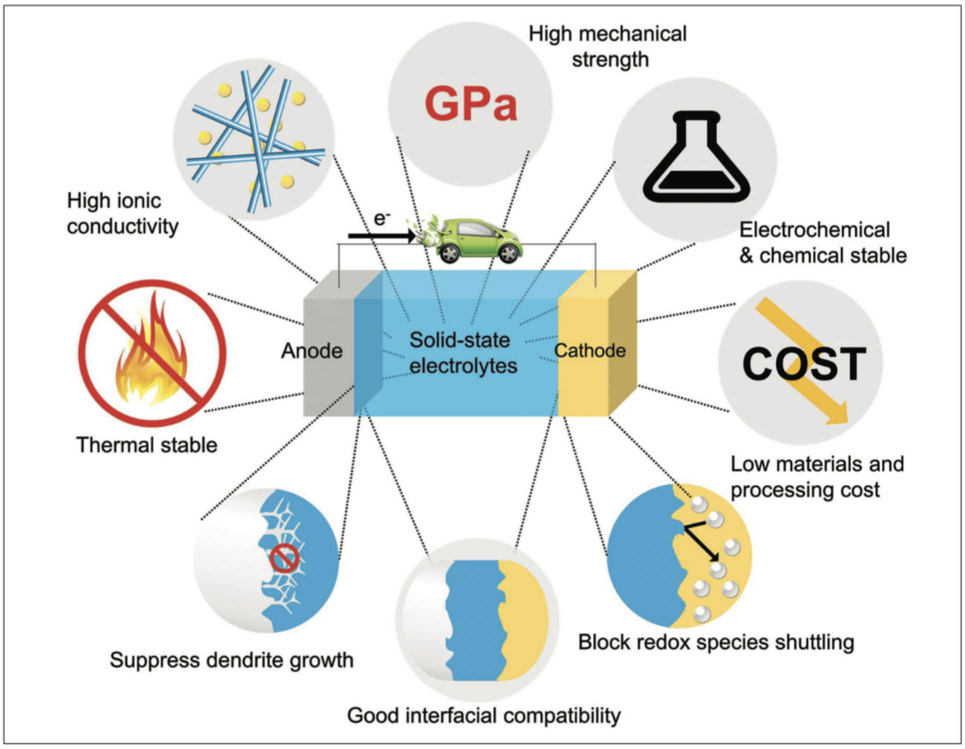

Figure 2.1: Main advantages of solid state batteries. Source: [9].

In addition to improved safety, SSBs provide the opportunity for significantly higher energy density. Solid electrolytes exhibit wide electrochemical stability windows and sufficient mechanical strength to suppress lithium dendrite growth, enabling the use of lithium metal as an anode. With a theoretical capacity nearly ten times greater than graphite as shown in Figure 2.2 and a very low redox potential, lithium metal represents the ultimate negative electrode. Coupling it with high-voltage cathodes could increase both the gravimetric and volumetric energy density of full cells, while also improving cycle life by limiting side reactions and degradation at the electrolyte–electrode interface [10].

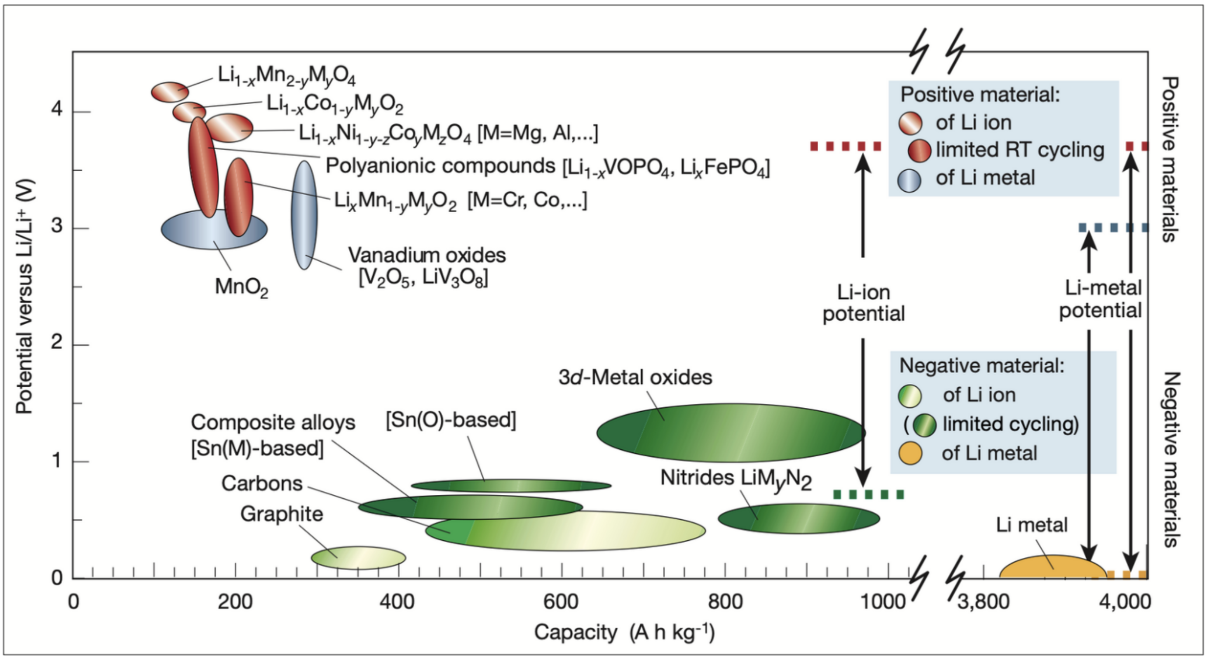

Figure 2.2: Relationship between energy density and operating voltage for different battery chemistries. Solid-state configurations with lithium metal anodes offer a clear advantage over conventional lithium-ion systems. Source: [8].

Different classes of solid electrolytes have been developed to realize these goals. Inorganic ceramics, including oxide families such as NASICON-type (LATP, LAGP) garnet-type $Li_7La_3Zr_2O_{12}$ (LLZO) and perovskites like $Li_{3x}La_{2/3-x}TiO_3$ (LLTO), offer high thermal stability and wide electrochemical windows. Sulfide electrolytes, exemplified by the Li_2S–P_2S_5 system, can achieve ionic conductivities comparable to liquid electrolytes and are processable at room temperature, though they are often sensitive to moisture, can release toxic gasses and have very limited electrochemical stability windows. Polymeric electrolytes, such as those based on poly(ethylene oxide) (PEO), are mechanically flexible and easy to process, but their conductivity is limited at ambient temperature. Hybrid systems combining ceramic fillers with polymer matrices attempt to combine the advantages of both approaches [10, 8].

Despite these advantages, key challenges remain before SSBs can achieve widespread commercialization. High interfacial resistance between solid electrolytes and electrodes limits rate capability and increases energy losses. Lithium dendrite penetration, though reduced compared to liquid systems, has also been reported in some ceramic electrolytes, compromising both safety and cyclability. Furthermore, processing dense ceramic membranes requires high-temperature sintering, which complicates scale-up and increases manufacturing cost. These issues currently represent the major bottlenecks for large-scale deployment [8].

Nevertheless, the progress achieved in recent years has pushed SSBs far beyond the laboratory stage. Several industrial groups, including Toyota, Samsung and Bosch, have announced prototype cells or pilot-scale production. Reported energy densities already exceed 800 Wh L^{-1}, substantially higher than current commercial lithium-ion batteries. While cost and manufacturability remain an open questions, these demonstrations confirm the potential of solid-state batteries to redefine the performance and safety standards of electrochemical energy storage [9].

2.2 Polymer-based electrolytes

Polymeric electrolytes represent one of the earliest and most extensively studied approaches to solid-state batteries. Interest in these systems was sparked in the late 1970s, when Wright demonstrated ionic conduction in poly(ethylene oxide) (PEO) and Armand proposed its application in electrochemical devices [1, 10]. In such materials, lithium salts dissolve into the polymer matrix, and cation transport is enabled by the coordination of Li^+ with electron-rich groups along the polymer chains. Studies established the feasibility of rechargeable lithium cells with polymer electrolytes, but also revealed the intrinsic limitation of low ionic conductivity at room temperature, typically below 10^{-5}S cm^{-1} [11].

Despite this drawback, polymer electrolytes offer several appealing features compared to both liquids and ceramics. They are lightweight, flexible, and easy to process into thin membranes, which makes them well-suited for compact devices. Their mechanical compliance ensures good contact with electrodes, reducing interfacial resistance. However, their limited electrochemical stability and the need for elevated operating temperatures restrict their compatibility with high-voltage cathodes and practical large-scale use [12].

Because of these advantages and limitations, polymer electrolytes have served as a platform for continuous innovation. From the early PEO-based systems to alternative polymer chemistries and the development of hybrid composite designs, research has sought to combine flexibility and processability with higher ionic conductivity and broader stability windows. The following sections will examine in more detail the main classes of polymer electrolytes: PEO-based systems, other polymer matrices, and other approaches including both polymers and inorganic compounds.

2.2.1 Polyethylene oxide

Poly(ethylene oxide) (PEO) is the most widely investigated polymer host for solid electrolytes, owing to its ability to solvate lithium salts through coordination of Li^+ with oxygen atoms along the polymer chain. This solvation mechanism ensures good salt dissolution and has made PEO the reference system for polymer-based electrolytes [11, 13]. The lithium-ion conductivity mechanism is represented in Figure 2.3.

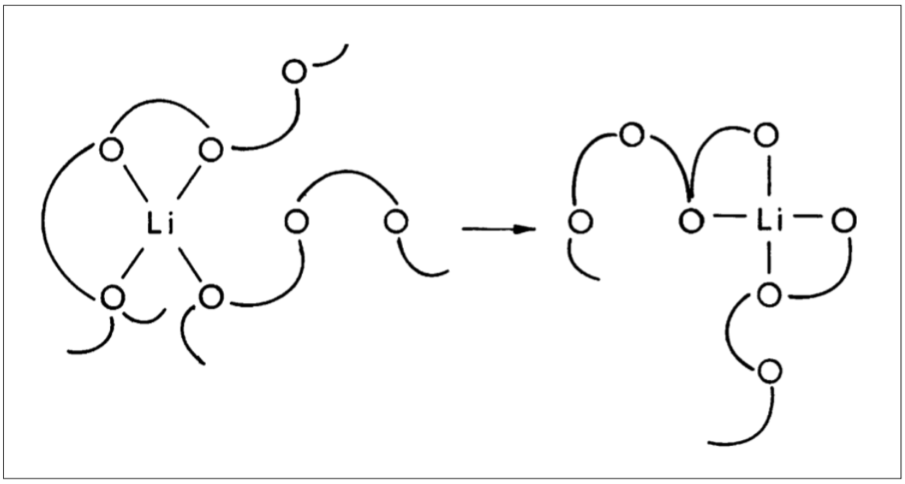

Figure 2.3: Li^+ conduction mechanism of PEO-based electrolytes. Source: [13].

Despite this advantage, the practical use of PEO is hindered by its low ionic conductivity at room temperature, typically below 10^{-5} S cm^{-1}. Ion transport in PEO is strongly coupled to the segmental motion of the polymer chains, and therefore occurs mainly in the amorphous phases while crystallization severely reduces conductivity, which is why most PEO-based electrolytes operate effectively only above 60 °C, where the polymer is predominantly amorphous [14].

Considerable effort has been devoted to improving the performance of PEO electrolytes. The choice of lithium salt plays an important role: salts with delocalized anions such as $TFSI^-$ or FSI^- reduce ion pairing and improve conductivity compared to $LiClO_4$ or $LiBF_4$ [13]. Conductivity values close to 10^{-4} S cm^{-1} at room temperature have been reported in optimized systems, particularly when combined with plasticizers or additives that suppress crystallinity [11].

Another strategy involves the design of block copolymers and polymer blends, which combine PEO segments for ion transport with mechanically robust backbones to enhance stability. More recently, PEO has also been employed as the polymer matrix in composite polymer electrolytes, further investigated in section 3.3.1, where the incorporation of ceramic fillers disrupts crystallinity and provides additional conduction pathways. These approaches demonstrate the versatility of PEO, but also underline its intrinsic limitations, as its conductivity and electrochemical stability remain below the levels required for high-voltage, room-temperature operation [14, 13].

2.2.2 Other polymers

Although PEO has dominated research on polymer electrolytes, many alternative polymers have been investigated to overcome its intrinsic limitations, either as standalone hosts or in combination with lithium salts and additives, to broaden the operating window of polymer electrolytes [13, 12].

Poly(vinylidene fluoride) (PVdF) and its copolymers, particularly PVdF-HFP, are among the most widely studied alternatives. They possess excellent electrochemical stability and mechanical strength, while their semi-crystalline structure provides both flexibility and dimensional stability. However, their low donor number means that they solvate lithium salts less effectively than PEO, so they are typically used in gel or composite electrolytes where ionic conductivity is enhanced by plasticizers or fillers [13].

Poly(acrylonitrile) (PAN) has also attracted attention thanks to its high polarity and strong interactions with lithium salts, which improve ionic transport. PAN-based electrolytes often exhibit higher room-temperature conductivity compared to PEO, but they can suffer from poor mechanical properties and limited long-term stability.

Poly(methyl methacrylate) (PMMA) has been investigated for its good electrochemical stability and ability to host large amounts of liquid plasticizers, making it suitable for gel polymer electrolytes, although its intrinsic conductivity remains lower than PEO and other polymers [11].

Other polymers such as poly(carbonate) (PC), poly(ethylene carbonate) (PEC), and various copolymers have also been explored. These systems often display improved stability or compatibility with lithium metal, but none have yet reached the balance of conductivity, stability, and processability required for practical applications. As a result, research increasingly focuses on combining different polymer chemistries to exploit their complementary strengths [13].

Table 2.1: Comparison of the most investigated polymer electrolytes for solid-state batteries [11, 13].

Polymer	**Advantages**	**Limitations**	**Typical Ionic Conductivity at 20°C**
PEO (polyethylene oxide)	Good Li salt solubility; well-studied; flexible	Low RT conductivity; high crystallinity; limited voltage window	$\sim 10^{-5}$ S cm^{-1}
PVDF (polyvinylidene fluoride)	Excellent electrochemical stability; good mechanical strength;	Poor Li$^+$ solvation; requires plasticizers or fillers	10^{-6} – 10^{-5} S cm^{-1}
PAN (polyacrylonitrile)	High polarity; good salt compatibility; decent RT conductivity	Poor mechanical stability; limited cycle life	10^{-5} – 10^{-4} S cm^{-1}
PMMA (polymethyl methacrylate)	Good electrochemical stability; hosts plasticizers well	Very low intrinsic conductivity; brittle without additives	$< 10^{-7}$ S cm^{-1}
PC (polycarbonate)	Wide electrochemical window; improved compatibility with Li metal	Moderate conductivity; limited mechanical robustness	10^{-6} – 10^{-5} S cm^{-1}

2.3 Alternatives to polymers as electrolyte materials

Although polymer electrolytes have long been investigated for solid-state batteries, their limited conductivity at room temperature and narrow electrochemical stability windows constrain their practical use. Inorganic ceramic electrolytes offer an attractive alternative, with ionic conductivities approaching those of liquid electrolytes (10^{-3}–10^{-2} S cm^{-1}), wide electrochemical windows, and superior thermal and chemical stability. However, ceramics are brittle, difficult to process into thin dense membranes, and often suffer from high interfacial resistance with electrodes [8, 10]. Table 2.2 shows the main advantages and limitations of the tree family of materials used in solid state batteries.

Table 2.2: Comparison of polymer, ceramic, and hybrid electrolytes for solid-state batteries.

Type	**Advantages**	**Limitations**
Polymers	Flexible, lightweight, easy processing, good electrode contact	Low RT conductivity, limited voltage stability, thermal sensitivity
Ceramics	High conductivity (10^{-4}–10^{-3} S cm^{-1}), wide electrochemical window, non-flammable, thermally stable	Brittle, costly processing, poor electrode interfaces
Hybrids	Combine flexibility of polymers with conductivity/stability of ceramics, improved interfaces	Performance depends on microstructure, complexity of fabrication

The following chapter will further elaborate on the working principles of ceramic electrolytes, main focus of this work, and provide an overview of the main families currently being studied and improved.

Chapter 3

Ceramic electrolytes

This chapter focuses on the most studied ceramic electrolytes for both sodium- and lithium-based systems in recent literature. These materials are mainly fabricated through glass-ceramic synthesis, the electrolyte can be made directly from crystallized glass drops or from sintered powders to allow for better shape adaptivness.

3.1 Sodium-conductive electrolytes

Sodium-conductive solid electrolytes are being developed as key components for sodium-ion batteries. Their role is to enable efficient Na^+ transport while maintaining chemical and electrochemical compatibility with both electrodes. By providing improved thermal stability and suppressing side reactions, solid electrolytes are expected to support the development of safe and durable sodium-based energy storage systems, unfeasible with a standard liquid electrolyte.

3.1.1 Anti-perovskites

Unlike lithium perovskites, which have been extensively studied, truly perovskite-type Na^+ conductors are not yet established. Instead, attention is focused on sodic anti-perovskite of general formula Na_3OX ($X = Cl, Br$, etc.), where the cation–anion positions are inverted compared to classical perovskites. In these frameworks, Na_6O octahedra form corner-sharing networks that provide pathways for Na^+ migration [5].

Recent studies report room-temperature ionic conductivities on the order of 10^{-3} S cm^{-1} and wide electrochemical stability windows above 5 V, making the material a promising candidate. Their high conductivity and mechanical strength suggest potential for dendrite suppression, a critical issue for sodium-metal systems. However, their high hygroscopicity requires careful handling, and their long-term chemical compatibility with sodium metal electrodes remains under investigation [5, 14].

3.1.2 Sodium sulfides

Sulfide-based sodium electrolytes have attracted increasing interest due to their high ionic conductivity and relatively low processing temperature. Their structural features-large ionic radius and high polarizability of sulfur-facilitate fast Na^+ transport, often reaching conductivities comparable to liquid electrolytes at room temperature [8, 9]. Among the most studied families are sodium thiophosphates, such as Na_3PS_4 and glass–ceramic derivatives obtained from mechanical milling or solution synthesis, which can achieve conductivities in the 10^{-3}–10^{-2} S cm^{-1} range [8]. Their soft mechanical character also enables intimate electrode–electrolyte contact, a major advantage compared to oxide ceramics [9].

Despite these benefits, sulfides suffer from limited stability in humid air, releasing toxic H_2S upon exposure, and from narrow electrochemical windows when in contact with high-voltage cathodes or sodium/lithium metal [8].

3.1.3 NASICON (Sodium super ionic conductor)

The first NASICON materials was first identified in the compound $Na_{1+x}Zr_2Si_xP_{3-x}O_{12}$ as a fast sodium ions conductor with a three-dimensional framework [15]. Since then, the NASICON family has been extensively investigated owing to its high structural stability, tunable composition, and ability to host a variety of alkali ions. Studied in both lithium and sodium analogues [7], the sodium-based systems are of particular interest for the development of cost-effective solid-state batteries, where abundant Na resources and stable frameworks are advantageous. Their versatility has also made NASICONs relevant for fuel cells, but their primary role today is as potential solid electrolytes in all-solid-state sodium-ion batteries [6]. A rappresntation of the NASICON lattice is shown in Figure 3.1.

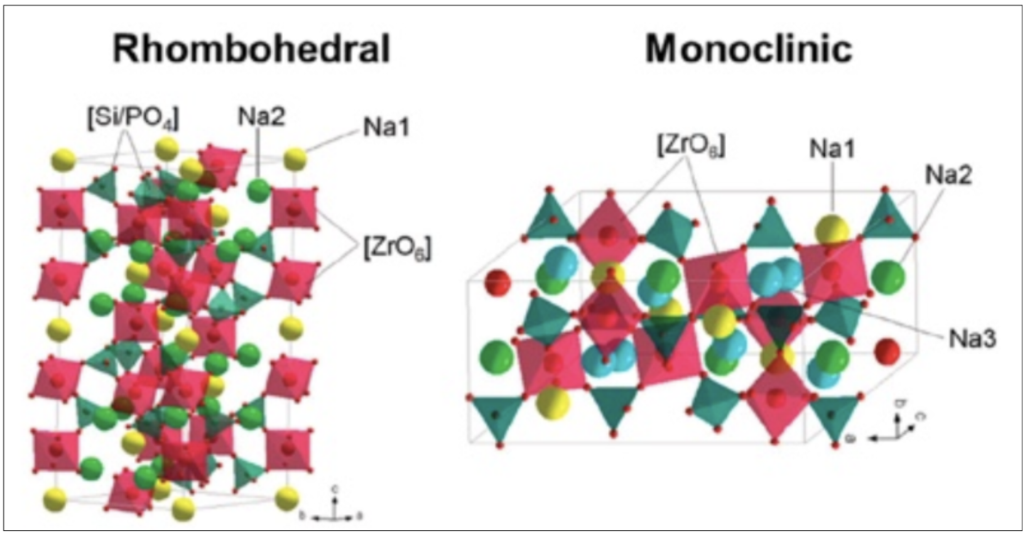

Figure 3.1: Crystal structure of NASICON in both the romboedral and monoclinc form. Adapted from [6].

The structure of NASICON is based on a rigid three-dimensional network of corner-sharing MO_6 octahedra (M = Zr, Ti, Ge, etc.) and PO_4/SiO_4 tetrahedra, which form so-called “lantern units” that repeat throughout the lattice. These lanterns connect to generate large interstitial sites and continuous tunnels that accommodate sodium ions. Two main types of Na sites are usually distinguished: type I sites, located within the channels, and type II sites, distributed around the framework. The partial occupancy of these sites, combined with the open connectivity of the framework, creates percolating conduction pathways [15].

A key advantage of NASICON is its compositional flexibility: the general formula tolerates a wide range of substitutions. Silicon and phosphorus can be partially replaced by other cations, while the zirconium site can accommodate dopants such as Ti, Ge, Hf, or Al. This adaptability enables fine-tuning of both stability and conductivity without disrupting the overall framework. Depending on composition and synthesis conditions, NASICON crystallizes in either a rhombohedral or a monoclinic form [6].

Mobile Na^+ ions migrate by hopping between type I and type II sites, following a three-dimensional percolation pattern [15]. This structural arrangement significantly lowers the activation energy compared to layered or one-dimensional conductors, resulting in fast ionic transport at elevated temperatures. Typical bulk ionic conductivities for well-optimized compositions reach values on the order of 10^{-3} to 10^{-2} S cm^{-1} at high temperature, although lower values are observed at room temperature [6]. A parallel can be drawn to the lithium NASICON analogues, which share similar framework features but display different site occupancies and mobility patterns [7].

In all-solid-state sodium-ion batteries, NASICON frameworks provide mechanical robustness, a wide electrochemical stability window, and compatibility with different electrode chemistries. These features make them particularly attractive for large-scale stationary storage, where cost and safety are critical considerations. Despite these advantages, NASICON electrolytes still face significant challenges. Grain boundary resistance can severely reduce the effective conductivity, while secondary phase formation during synthesis may further limit performance. At the electrode–electrolyte interface, stability against metallic sodium is a major concern. Similar to lithium systems, sodium metal anodes are prone to dendrite growth and the formation of unstable solid electrolyte interphases, which compromise both safety and efficiency [5]. As depicted in Figure 3.2, solid electrolytes such as NASICON can mitigate dendritic growth to some extent by providing mechanical resistance, but they are not immune to penetration through structural defects or grain boundaries.

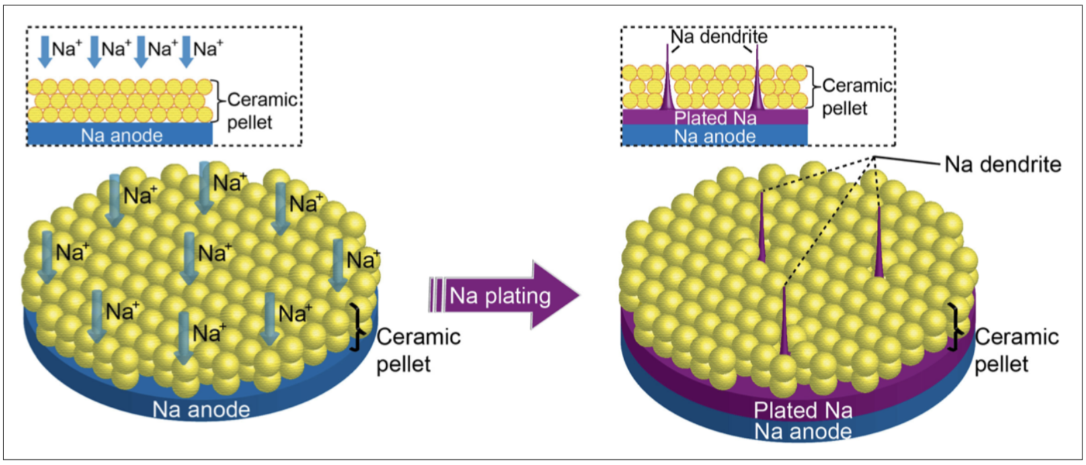

Figure 3.2: Schematic representation of sodium metal anode dendrite growth on a solid electrolytes such as NASICON. Adapted from [16].

3.2 Lithium-conductive electrolytes

This section is dedicated to a literature review of lithium conductive ceramic electrolytes, which represent the main focus of the experimental work carried out in this thesis. The discussion will cover the main families investigated in the field, namely sulfides, perovskites, garnet-type and NASICON-type electrolytes.

3.2.1 Li^+ conductive Perovskites

Perovskite-type oxides, such as lithium lanthanum titanate ($Li_{3x}La_{2/3-x}TiO_3$, LLTO), are a well-established family of lithium-ion conductors. Their structure consists of corner-sharing TiO_6 octahedra with large A-site channels partially occupied by La^{3+} and Li^+, enabling fast Li^+ migration through bottlenecks in the perovskite lattice [8, 17]. Reported conductivities exceed 10^{-3} S cm^{-1} at room temperature, making them competitive.

The principal limitation of LLTO arises from its chemical instability against metallic lithium: at low potentials, Ti^{4+} is reduced to Ti^{3+}, resulting in eventual short-circuiting [17]. Moreover, large grain boundary resistances often dominate the total impedance, especially in polycrystalline ceramics [8]. To address these drawbacks, approaches such as doping, composite engineering, and protective interlayers have been investigated. While unlikely to be used directly with Li metal anodes, LLTO and related perovskites may find application in hybrid solid-state battery architectures.

3.2.2 Lithium sulfides

Sulfide-based solid electrolytes have attracted considerable attention thanks to their outstanding lithium-ion conductivities, in some cases exceeding 10^{-2} S cm^{-1} at room temperature, which is on par with liquid electrolytes [8, 9]. The breakthrough came with the thio-LISICON family, where substituting oxygen with sulfur in LISICON-type structures expanded the lattice and lowered the migration barrier for Li^+, leading to superionic transport [14]. This class was further developed into glass–ceramic thiophosphates, such as $Li_{10}GeP_2S_{12}$ (LGPS), which remain among the fastest known lithium-ion conductors [10].

A distinctive advantage of sulfides compared with oxides is their relatively soft mechanical nature. Their low elastic modulus allows intimate interfacial contact with electrodes during pressing or sintering, minimizing grain-boundary resistance and enabling dense composite cathodes. This property has made sulfides particularly attractive for high-power applications [8].

Nevertheless, critical challenges limit their widespread adoption. Chemically, sulfides are unstable in ambient conditions, reacting with moisture to form H_2S gas, which complicates handling and large-scale processing [12]. Electrochemically, they often exhibit narrow stability windows: reduction at the lithium anode side leads to resistive interphases and potential dendrite growth, while oxidation at high-voltage cathodes causes decomposition. Protective coatings, buffer layers, and compositional modifications (e.g., partial oxygen substitution) are therefore under active investigation to extend their compatibility [9].

3.2.3 Garnet-type

Garnet-type oxides, particularly lithium lanthanum zirconium oxide ($Li_7La_3Zr_2O_{12}$, LLZO), have emerged as highly promising candidates for solid-state lithium batteries. Their crystal structure enables three-dimensional Li^+ transport, and the cubic polymorph, of which the structure and conductive path is shown in Figure 3.3 can reach room-temperature ionic conductivities close to 10^{-3} S cm^{-1} [18, 9]. In contrast, the tetragonal phase shows conductivities two orders of magnitude lower, making stabilization of the cubic phase essential.

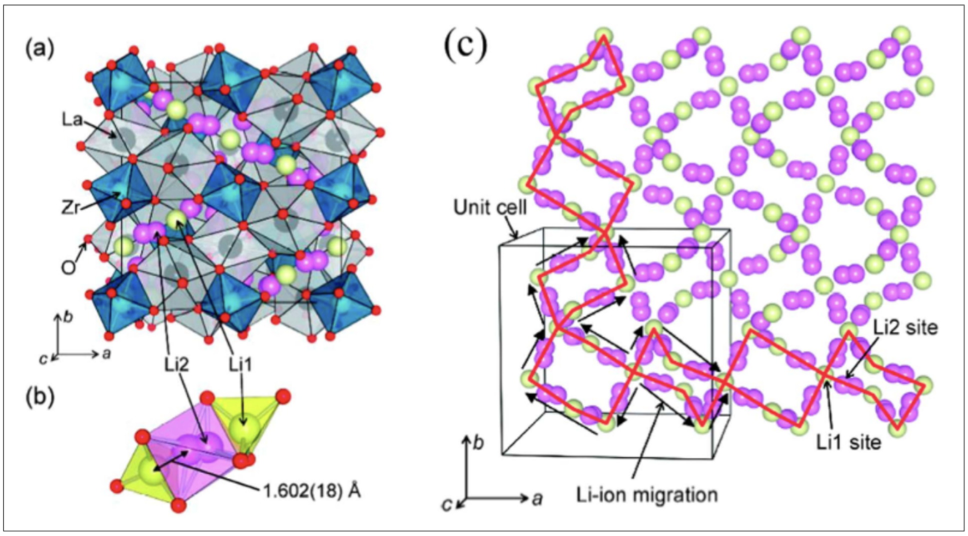

Figure 3.3: (a) Crystal structure of cubic $Li_7La_3Zr_2O_{12}$, (b) Coordination polyhedra around the Li1 and Li2 sites; (c) Three-dimensional conducting network of the Li-ion in cubic $Li_7La_3Zr_2O_{12}$. Source: [19].

Aliovalent doping is the most effective strategy to stabilize cubic LLZO. Al, Ga, Ta, and Nb substitutions introduce lithium vacancies and lattice disorder that promote ionic mobility [18]. For instance, Ga-doped LLZO prepared from micron-sized powders achieved a relative density above 95% and conductivity of 5.6×10^{-4} S cm^{-1} after short sintering at 1180 °C [20]. Optimized Al- and Ta-doped LLZO compositions have reported conductivities up to $\sim 1 \times 10^{-3}$ S cm^{-1} at room temperature [18].

Surface chemistry also plays a decisive role. Exposure to ambient air leads to the formation of Li_2CO_3, which increases interfacial resistance with lithium metal. Ultrafast laser processing has been shown to effectively remove this insulating layer, lowering the Li/LLZO interfacial resistance by about 94% [21]. Despite their chemical stability against Li metal, garnet-type electrolytes typically exhibit limited oxidative stability, restricting their compatibility mainly to medium-voltage cathodes.

3.2.4 NASICON-type

NASICON-type materials are among the most studied oxide solid electrolytes for lithium-ion conduction. Their crystal structure, similar to Na^+ conductive NASICON, based on MO_6 octahedra linked with PO_4 tetrahedra, creates a three-dimensional network with bottlenecks that enable fast Li^+ transport [22]. This family includes $Li_{1+x}Al_xTi_{2-x}(PO_4)_3$ (LATP), $Li_{1+x}Al_xGe_{2-x}(PO_4)_3$ (LAGP), and mixed Ti,Ge or other metals solid solutions such as LAGTP and LAMGP. A visual representation of the 3D Li^+ conductive structure of LAGP/LAMGP material is shown in figure 3.4.

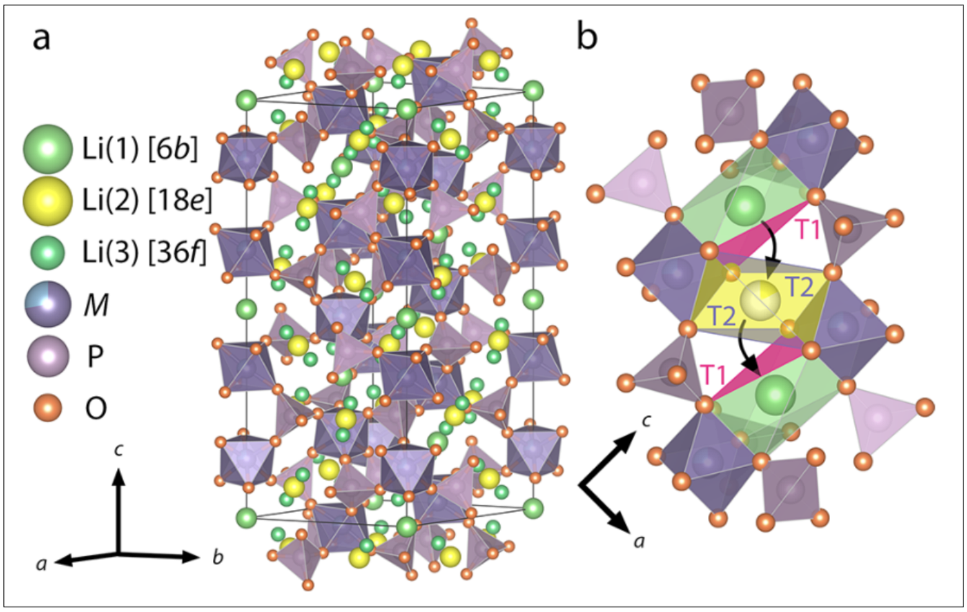

Figure 3.4: (a) Polyhedral representation of the crystal structure of $Li_{1+x}Al_xTi_{2-x}(PO_4)_3$ (M = Al/Ge). (b) Visualization of the hopping path of Li^+ through the two triangle areas T1 and T2 according to Tietz and co-workers [23]. Source:[22].

LATP has been widely investigated due to its relatively high ionic conductivity, with reported values around $3\text{–}5\times10^{-4}$ S cm^{-1} at room temperature, increasing to $\sim 10^{-3}$ S cm^{-1} at higher temperatures [24, 25]. It also shows excellent air and moisture stability, making it suitable for practical handling. However, LATP suffers from chemical instability against metallic lithium, where reduction at the interface leads to resistive interphases. Processing is also challenging, since LATP requires high sintering temperatures that often result in lithium evaporation and secondary phase formation [24, 25].

LAGP, obtained by substituting Ti^{4+} with Ge^{4+}, generally exhibits similar or higher conductivities, in the 10^{-4}–10^{-3} S cm^{-1} range at room temperature [22]. It is considered more stable than LATP toward lithium metal, although interfacial resistances remain significant. In addition, the high cost and scarcity of germanium limit large-scale adoption. Synthetic approaches strongly affect LAGP's performance: conventional melt-quenching requires high temperatures, while aqueous synthesis routes are emerging as simpler and less expensive alternatives [22].

Mixed systems, such as LAGTP and LAMGP, have been investigated to combine and improve the advantages of both LATP and LAGP. These compositions typically display room-temperature conductivities in the 10^{-4} S cm^{-1} range and maintain good structural stability [26, 27]. While they do not fully solve the interfacial and processing issues, they highlight the compositional flexibility of the NASICON framework and show the higher anodic stability among all ceramic conductors.

3.3 Improvement strategies

All materials listed in section 2.2 and 3.2 are promising but have also intrinsic limitations as they do not provide sufficient ionic conductivity or interfacial stability. For this reasons different strategies are being developed to enhance the materials properties, following two main routes: improvement of the solid ceramic or combination of polymers and ceramic in a composite material.

3.3.1 Hybrid electrolytes

Hybrid electrolytes represent an intermediate class of solid-state ionic conductors, designed to bridge the gap between purely inorganic ceramics and polymer-based systems. They are generally obtained by combining a polymer matrix with dispersed inorganic fillers, which acts as mechanical reinforcements, suppressing dendritic growth while also contributing to lithium-ion conduction [28]. This approach aims to combine high interfacial contact with electrodes, typical of polymer electrolytes, with the mechanical robustness and wider electrochemical stability window of ceramic materials. By reducing the crystallinity of the polymer host and providing additional transport pathways, inorganic fillers can enhance ionic conductivity, often allowing room-temperature operation in systems where polymers alone would be insufficient [29]. However the distribution and compatibility of ceramic fillers within the polymer matrix are critical: poor dispersion or weak interfaces can create inhomogeneities, blocking transport instead of facilitating it. High filler contents, while beneficial for conductivity, can compromise flexibility and processability [28]. Recent works have demonstrated different approaches to hybrid electrolytes, each targeting improvements in conductivity, stability, or compatibility with electrodes.

Kirianova *et al.* investigated composite gel–polymer electrolytes incorporating nanosized LATP fillers. They showed that the filler size is a key parameter: particles around 50 nm provided the best combination of transport and mechanical integrity. The optimized composite achieved an ionic conductivity of approximately 1×10^{-3} S cm^{-1} at room temperature, supporting stable operation even under high current densities [28].

Yu *et al.* developed a single-ion conducting polymer–LATP composite based on sulfonated polyoxadiazole. Although the conductivity was lower ($\sigma \approx 2 \times 10^{-4}$ S cm^{-1} at room temperature), the electrolyte delivered a lithium-ion transference number close to 0.82 and excellent electrochemical stability. Symmetric Li||Li cells operated for more than 2400 h at 1 mA cm^{-2} with a stable overpotential of ~12 mV, while full cells using LFP and NCM811 cathodes retained 85% of their initial capacity after 500 cycles, underlining the durability of single-ion hybrid systems [29].

3.3.2 Doping effects

As an alternative to hybrid systems fully ceramic system are also being improved with different strategies. Overall for certain NASICON-type ceramics, bulk crystallized glass shows better properties compared to the powder sintered counterparts that however allow for much easier processability, which makes it object of most studies as it is more likely to be a scalable technology.

The use of dopants in NASICON-type materials such as LAGP, LATP and LAMGP is primarily aimed at improving densification and ionic transport. One of the most effective strategies consists in introducing sintering aids that generate a transient liquid phase during heat treatment. These liquid phases wet grain boundaries, enhance particle rearrangement, and foster grain-to-grain cohesion, thereby reducing porosity and grain boundary resistance, main obstacle for Li-ions transport. Although the dopants themselves are usually electronically insulating, their role in improving microstructure has a decisive impact on improving overall ionic conductivity. A few of the latest works on the subject are presented.

He et al. studied in an early work the role of Al_2O_3 additions in LAGP systems, observing a complex balance between secondary $AlPO_4$ formation and conductivity enhancement when the Al content was optimized [30]. Further studies reported that also trivalent cations such as Ga^{3+}, Sc^{3+} or Y^{3+} can improve bulk ionic conductivity in LATP by introducing disorder and vacancies in the NASICON structure [26].

Jadhav *et al.* studied the incorporation of small amounts of B_2O_3 into LAGP glass-ceramics prepared by melt-quenching and subsequent crystallization [31]. A nominal content of 0.05 wt% B_2O_3 was sufficient to significantly alter the sintering behavior, lowering the crystallization temperature to 825 °C and enabling finer, more uniform microstructures. Impedance measurements showed an ionic conductivity (at 25°C) of $6.94 \times 10^{-4}\,\mathrm{S\,cm^{-1}}$, which is among the highest reported for oxide NASICONs. However, at larger B_2O_3 contents (>0.1 wt%), the segregation of resistive glassy phases at grain boundaries became detrimental, reducing the overall conductivity.

Saffirio *et al.* investigated the addition of diboron trioxide (B_2O_3) to LATP glass-ceramics [26]. They demonstrated that the amorphous borate, melting at relatively low temperature, segregates at grain boundaries during devitrification. This process resulted in enhanced densification and in a marked improvement of Li^+ conductivity compared to undoped LATP, reaching the value of $3.4 \times 10^{-4}\,\mathrm{S\,cm^{-1}}$. The study highlighted the effectiveness of boron-based additives in forming a liquid-assisted sintering pathway without generating parasitic crystalline phases.

The same group (2024) performed a systematic comparison of different dopants (Y_2O_3, B_2O_3, SiO_2) in LAMGP glass-ceramics, showing that Y_2O_3 and B_2O_3 significantly improve grain cohesion, while SiO_2 tends to induce microcracks and reduce ionic transport [27]. The addition of Mg to the structure serve the purpose of creating extra vacancies to allow for better Li-ions transport, hence reducing bulk resistance, however it delivers no effect on the grain boundary resistance. Notably, B_2O_3 was found to segregate at grain boundaries without altering grain shape or introducing insulating crystalline impurities, unlike Y_2O_3, which produced YPO_4 phases. This approach allowed to obtain a sample doped with B_2O_3 with a room-temperature ionic conductivity value of 2.1×10^{-4}. Although this phase is intrinsically insulating, its presence enhances densification and grain cohesion so effectively that the overall ionic conductivity of LAMGP glass-ceramics increases dramatically.

Bai *et al.* investigated the effect of lithium borate on LATP ceramics by adding $LiBO_2$ as a sintering aid [25]. The powders were synthesized by solid-state reaction, and 1.0 wt% $LiBO_2$ was introduced before sintering at 800 °C. The additive promoted transient liquid-phase sintering, resulting in improved densification and a relative density of 97.1%. Electrochemical impedance spectroscopy revealed a sharp reduction in grain boundary resistance, leading to a room-temperature ionic conductivity of $3.5 \times 10^{-4}\,\mathrm{S\,cm^{-1}}$. At higher

$LiBO_2$ contents (1.5–2.0 wt%), secondary $Li_4P_2O_7$ phases were detected, which compromised both density and conductivity.

Sabato *et al.* examined the role of Li_3BO_3 as a sintering additive in LAGP systems, processed both conventionally and via ultrafast high-temperature sintering (further explained in Section 3.3.3) [32]. In both cases, the lithium borate promoted partial liquid-phase sintering, improving grain cohesion and reducing intergranular resistance without forming parasitic crystalline phases. The best samples displayed a room-temperature ionic conductivity of $2.3 \times 10^{-4}\,\mathrm{S\,cm^{-1}}$, higher than that of undoped LAGP but slightly lower than B_2O_3-doped analogues. The authors emphasized that Li_3BO_3 remains a useful flux, particularly under rapid sintering, although its effect is less pronounced than that of pure B_2O_3.

3.3.3 Unconventional sintering strategies

Conventional sintering of NASICON-type glass–ceramics typically requires long dwell times at high temperatures (700–1000 °C), which promotes lithium volatilization and secondary phase formation. To overcome these limitations, several alternative approaches have recently been developed, aiming to reduce processing time, energy demand, and defect formation while maintaining high density and ionic conductivity. The following studies illustrate the most relevant strategies.

Zhou *et al.* (2025) proposed a two-step sintering approach combined with LATP glass nanoparticle additives [33]. In this method a composite powder of LATP glass and LATP ceramic was used. During the first sintering step a viscous flow generated by the glass phase enhances densification, while controlled crystallization in the second step applies compressive stresses that suppress abnormal grain growth and generate uniform-sized grains. To prepare fine powders, a melt and quench process was used to obtain glassy LATP (∼80 nm) and solid-state reaction for crystalline LATP (∼600 nm), both further milled for homogeneity. This dual-powder system yielded dense ceramics with relative density above 95% and room-temperature ionic conductivity of $\sim 7.3 \times 10^{-4}$ S cm^{-1}.

Saffirio *et al.* (2025) applied ultrafast high-temperature sintering (UHS) to LAMGP +0.5 % B_2O_3 compositions [34], following the same steps used by Sabato and co-workers [32]. In this setup, glass powders were placed between carbon felts crossed by high currents, inducing Joule heating at rates up to 10^5 °C min^{-1}. Full densification was achieved in only 3 min, with density values comparable to conventional long sintering. Importantly, UHS suppressed lithium volatilization and prevented secondary phase formation, resulting in room-temperature conductivities above 2×10^{-4} S cm^{-1}. The addition of B_2O_3 further reduced grain boundary resistance by segregating at interfaces, improving ionic transport.

Chapter 4

Materials and Methods

Previous works [27] showed the effectiveness of different additives, such as yttrium or boron oxide, in increasing the ionic conductivity of LAMGP ceramics. B_2O_3 in particular appears to be the most effective at increasing grain cohesion and size, hence reducing grain boundary resistance [26].

B_2O_3 is an ionic insulator, however, because of its low melting point, it causes the formation of a liquid transient phase during the crystallization of LAMGP, filling most of the voids in the material, hence an major increase in ionic conductivity.

Using lithium borates instead of B_2O_3 could be a promising approach to replicate the same grain cohesion with a phase that also contains lithium, thereby increasing free lithium ions for conduction and mitigating lithium loss above 700 °C [35].

In this work I studied the effect of lithium metaborate and tetraborate addition to the same LAMGP material previously studied [26, 34], using similar processing methods and characterization techniques.

4.1 $Li_2B_4O_7$ synthesis

$Li_2B_4O_7$ was not available at the supplier and therefore it was synthesized following the solution-assisted synthesis route developed by Pekpak et al. [36] with slight modifications. Lithium carbonate and boric acid were dissolved in water in stoichiometric amounts to allow the formation of $Li_2B_4O_7$ according to the following reaction:

$$\mathrm{Li_2CO_3(s)} + 4\,\mathrm{H_3BO_3(s)} \longrightarrow \mathrm{Li_2B_4O_7(s)} + \mathrm{CO_2(g)} + 6\,\mathrm{H_2O(g)} \tag{4.1}$$

The solution was stirred and heated to ∼200 °C until nearly complete evaporation occurred, resulting in the formation of a slurry. This slurry was then further dried in a furnace at 150 °C for 3 hours to promote dehydration. The powder obtained at this stage was partially amorphous. In contrast to the original method, the dried precursor was then pressed into pellets and placed on an alumina plate in a furnace at 750 °C for 2 h to promote crystallization. The crystallized $Li_2B_4O_7$ shown in Figure 4.1 exhibited a "popcorn-like" morphology, likely due to residual water evaporation during heating. Finally, the material was ground in a mortar to obtain a fine powder.

Figure 4.1: Morphology of synthesized $Li_2B_4O_7$.

The crystallinity and purity of the synthesized $Li_2B_4O_7$ were evaluated by XRD analysis.

4.2 Samples preparation

4.2.1 Glass casting

The electrolytes have been prepared by glass-ceramic synthesis following the procedure used by Saffirio et al. [27], with B_2O_3 replaced by $LiBO_2$ and $Li_2B_4O_7$. Based on the target compositions, reagent amounts were calculated to obtain 40 g of $Li_{1.5}Al_{0.3}Mg_{0.1}Ge_{1.6}(PO_4)_3$ glass containing 0.5 wt% $LiBO_2$ and 10 g of glass containing 0.5 wt% $Li_2B_4O_7$. To account for lithium volatilization at high temperature, excess Li_2CO_3 was added to the batch composition. Following the procedure reported by Brewer and Margrave [35], Saffirio et al. [27] introduced a small excess (0.5 wt%) of Li_2CO_3 in order to compensate for lithium loss during melting at 1350 °C. However, in the work, lithium depletion was still detected. For this reason, a larger excess was employed: 3.75 wt% of Li_2CO_3 was added to the starting mixture to ensure full lithium incorporation, while maintaining the nominal stoichiometry of the final LAMGP composition. This adjustment was necessary to stabilize the NASICON framework and minimize the formation of secondary GeO_2 phases during, resulting from Li volatilization. Higher amounts were not employed as they could cause the formation of Li_2O if the addition is larger than the volatilization during sintering. The standard LAMGP composition is listed in Table 4.1 while the amounts of reagents in moles and mass for the two modified compositions are listed in Table 4.2.

Table 4.1: LAMGP molar composition.

Oxide	moles
Li	1.5
Al	0.3
Mg	0.1
Ge	1.6
P	3

Table 4.2: Amounts of precursor reagents required to obtain 10 and 40g of LAMGP + 0.5 wt% $LiBO_2/Li_2B_4O_7$.

Reagent	moles for 10g	mass(g) for 10g	mass(g) for 40g
Li_2CO_3	0.071	1.69	6.75
Al_2O_3	0.014	0.36	1.45
$MgCO_3$	0.009	0.20	0.80
GeO_2	0.152	3.97	15.87
$NH_4H_2PO_4$	0.284	8.18	32.70
$LiBO_2$ or $Li_2B_4O_7$	-	0.05	0.20

Precursors were mixed for 24 hours and then placed in an alumina crucible inside a casting furnace (Nabertherm 1800) and heated up according to the heating profile reported in Table 4.3. The setup of the furnace is shown in Figure 4.2, the alumina crucible was partially covered to avoid contaminating the furnace but at the same time allow CO_2 and NH_3 to escape.

Table 4.3: Melting/heating schedule.

Step	Heating rate (°C/min)	Time (min)	Temperature (°C)
1	10	-	20-350
2	0	30	350
3	10	-	350-700
4	0	30	700
5	10	-	700-1350
6	0	60	1350

The heating profile included 30 min isothermal holds at 350 °C and 700 °C to enable, respectively, the release of NH_3 from $NH_4H_2PO_4$ and the decomposition of Li_2CO_3 with CO_2 release.

The reactions happening at each temperature are the following:

$$2\,NH_4H_2PO_4 \longrightarrow P_2O_5 + 2\,NH_3 + 3\,H_2O \tag{4.2}$$

$$Li_2CO_3 \longrightarrow Li_2O + CO_2 \tag{4.3}$$

A final hold at 1350 °C for 1 h ensured complete melting and homogenization. The melt was cast dropwise onto a brass plate (Figure 4.3) to promote rapid quenching. In contrast to the original method, no post-quench annealing was performed at 470 °C.

Figure 4.2: Furnace setup for glass casting.

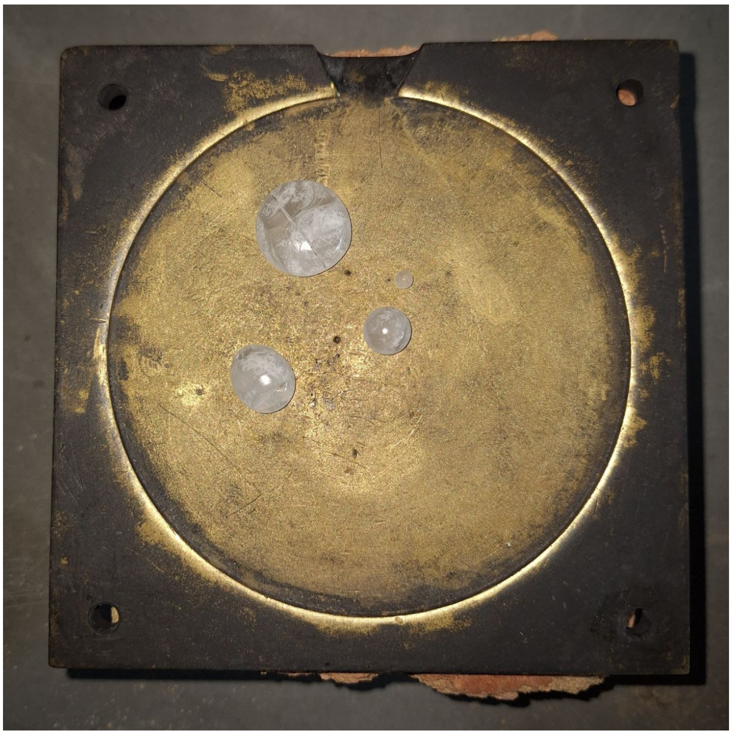

Figure 4.3: Quenched glass drops.

4.2.2 Bulk samples

Some quenched drops were thermally treated in an oven (Nabertherm 1300). The samples were heated at a rate of 5 °C/min up to Tg + 20 °C at which they were held for 1 hour to promote nucleation. The value of Tg was determined by DSC analysis, as described in Section 4.3.1. After this step, heating was continued at the same rate up to 700 °C, where the samples were maintained for 12 hours to enable grain growth.

The crystallized glass was then polished using low-grit (150-600) SiC abrasive paper on a polishing machine in order to reshape it and obtain a more uniform thickness of about 0.8 mm. This step was necessary because the ceramic sample is required to fit between two cell electrodes for electrochemical testing, which requires minimal thickness variation and the largest possible contact area. The reshaped sample is shown in Figure 4.4.

Figure 4.4: Reshaped and polished bulk LAMGP specimen.

4.2.3 Sintered samples

The remaining drops were first milled in a ball milling machine (Retsch MM400) using zirconia jars and balls. The powders were then sieved through a 38 μm mesh using an automatic sieving machine for 1 hour. For the coarse fraction, the milling procedure was repeated, as well as the sieving, to recover as much material as possible. The powders were then pressed at 100 bar for 2 min to form round pellets, each containing roughly 0.5 g of glass. The samples were then positioned on an alumina plate, sintered and crystallized in an oven (Nabertherm 1300). For most of the samples, the same thermal treatment used by Saffirio and co-workers [27] was applied, with heating at 5 °C/min until reaching 700 °C, at which they were held for 12 h. Higher sintering temperatures were investigated for both compositions: 850 °C for the system containing $LiBO_2$, and 920 °C for the system containing $Li_2B_4O_7$. The reason for this is that these sintering temperatures are just above the melting points of $LiBO_2$ and $Li_2B_4O_7$, thus favoring the formation of transient liquid phases and potentially improving grain cohesion according to the same reasoning applied in previous studies with B_2O_3 (melting at 450 °C) [26][27][34]. The sintered samples, shown in Figure 4.5, have the advantage of being perfectly round compared to the bulk ones.

Figure 4.5: Sintered LAMGP pellets.

4.2.4 Polishing and preparation for electrochemical testing

All samples, both bulk and sintered, were then polished on a polishing machine using different SiC abrasive papers ,ranging from 600 to 4000 grit, to achieve a uniform thickness and reduce surface roughness, thereby increasing the effective surface contact area in the stainless steel electrochemical cell. All samples were sputtered with Au to create a 50 nm layer on the surface, on both faces for the samples destined to EIS and on one face only for the ones destined for ESW, leveraging gold malleability to ensure optimal contact with the electrodes. A ready-to-test sample is shown in Figure 4.6.

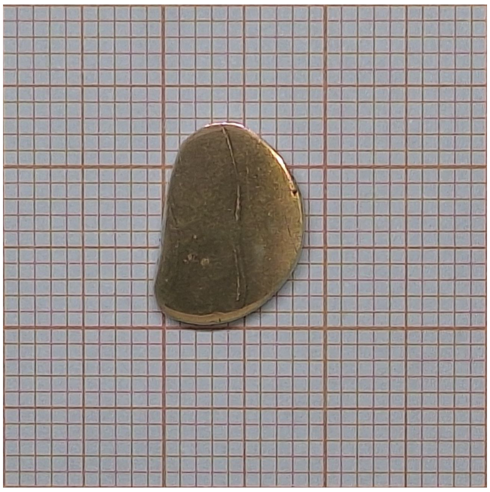

Figure 4.6: Sample prepared for electrochemical testing.

4.3 Characterization techniques

4.3.1 Differential scanning calorimetry

The thermal behavior of the investigated glass–ceramic compositions was studied by Differential Scanning Calorimetry (DSC, Netzsch 404 F3 Pegasus, Germany). DSC is a thermoanalytical technique that records the difference in heat flow between a sample and an inert reference as a function of temperature or time, thus providing valuable information on phase transformations, crystallization events, and thermal stability. In the case of glass and glass–ceramic materials, it allows the determination of characteristic transition points, such as the glass transition temperature (Tg), the onset and peak crystallization temperatures (Tx), and melting temperature (Tm).

For the present work, the measurements were carried out in the temperature range of 25–1000 °C, inside Pt-Rh crucibles, under a controlled heating program in synthetic air atmosphere. A constant heating rate of 5 °C·min^{-1} was applied to ensure reproducibility and adequate resolution of the thermal events. The obtained DSC thermograms enabled the identification and comparison of the main thermal transitions associated with the LAMGP powders modified with $LiBO_2$ and $Li_2B_4O_7$.

4.3.2 Hot-stage microscopy

Sintering behavior of the glass–ceramic powders was examined by Hot Stage Microscopy (HSM, Hesse Instruments, EM301). The powders were uniaxially pressed into small pellets (few mm) and placed in the furnace chamber of the instrument, where the temperature was precisely monitored by a thermocouple. The furnace, equipped with water cooling and capable of operating under controlled atmosphere, was programmed to follow the selected heating ramp.

Hot Stage Microscopy (HSM) consists of placing the sample in a heated chamber, where it is illuminated and continuously observed by a digital camera. As the temperature increases, the images recorded by the camera enabled real-time monitoring of dimensional changes (shrinkage, swelling, melting) as a function of temperature. Image analysis of these recordings enabled the evaluation of dimensional variations (area and height), directly reflecting the shrinkage of the sample. This allows the identification of characteristic sintering temperatures, including the softening, spherical, hemispherical, and flow points.

In this study, LAMGP powders were analyzed in the temperature range of 25–1100 °C with heating rates of 5-10 °C·min^{-1}. The method provided direct insight into the densification process and enabled comparison of the thermal behavior of the two compositions as well as the evaluation of the shrinkage by calculating the surface area of images at different temperatures.

4.3.3 Crystalline phase analysis by X-ray diffraction

The crystalline phases of the sintered glass-ceramic samples were examined by X-ray diffraction (XRD, Bruker D8 ADVANCE, Germany). This technique relies on the interaction between incident Cu Kα radiation ($\lambda = 1.5406$ Å) and the periodic atomic structure of the material, producing diffracted beams that satisfy Bragg's law. The resulting diffractograms, recorded as intensity versus diffraction angle (2θ), allow the identification of the crystalline phases present and provide insight into the crystalline evolution of the samples after sintering.

In this study, the measurements were carried out at room temperature under operating conditions of 40 kV and 40 mA. Data were collected in the 2θ range of 10–70°, which was sufficient to resolve the principal diffraction peaks associated with the crystalline phases formed in the investigated compositions.

4.3.4 Sample imaging for area measurement

To calculate the ionic conductivity of the samples, precise measurement of the contact area and thickness are required. Since some of the samples were not perfectly round, the area was determined by pixel counting from photographs of the samples.

To avoid distortions that can occur with a standard camera, the samples were placed next to millimetric paper, used as a reference, and photographed using a commercial flatbed scanner. The resulting images are shown in Figure 4.7. The sample area was then converted into cm^2 using the reference scale. Samples 23, 20, 8 and 5 had already been metallized when the image was acquired, explaining the gray color compared to the white of the others.

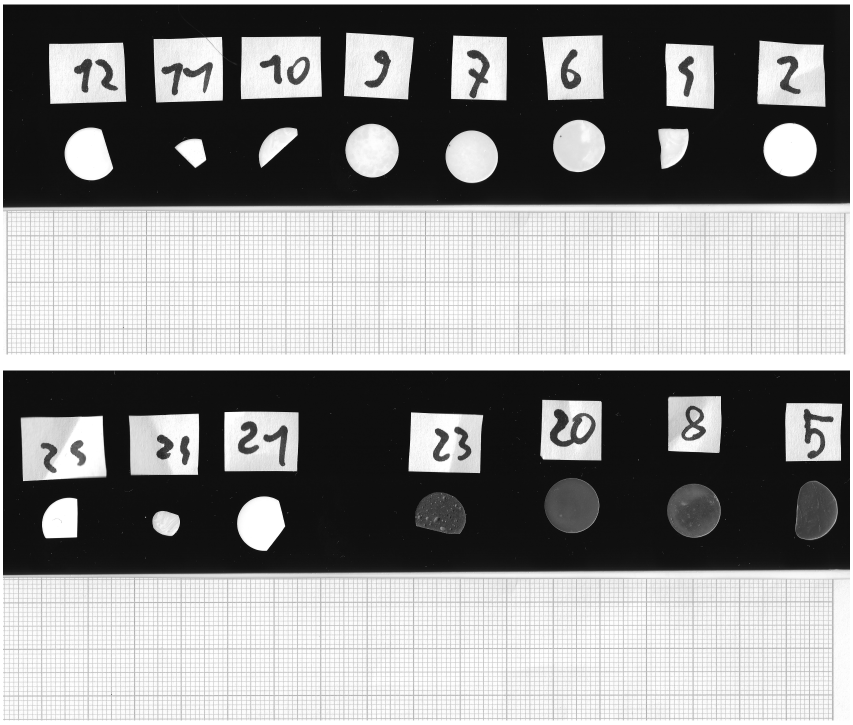

Figure 4.7: Images of samples acquired with a flatbed scanner.

4.3.5 Density by Archimedes' method

Density was measured by the Archimedes method (ASTM C373). Mass was recorded in air and in ethanol (99%), then converted to density via the following equation:

$$\rho = \frac{m_{\mathrm{air}}}{m_{\mathrm{air}} - m_{\mathrm{liq}}} \cdot \rho_{\mathrm{liq}} \tag{4.4}$$

Ethanol was preferred over water (used by Saffirio and co-workers [26]) for faster drying, allowing for repeated measurements on the same specimen.

4.3.6 SEM imaging and porosity evaluation

The microstructure of glass–ceramic electrolytes plays a key role in determining their ionic conductivity, since defects such as grain boundaries, pores, and cracks can compromise ion transport. Scanning Electron Microscopy (SEM) is a powerful technique that allows direct observation of surface morphology at the micrometric scale.

SEM works by scanning a focused beam of electrons over the sample surface. The interaction between the electrons and the material produces various signals, of which the secondary electrons one is collected to generate high-resolution images of surface morphology. Energy-Dispersive X-ray Spectroscopy (EDS), based on the detection of characteristic X-rays, can be coupled with SEM to obtain information on the elemental composition of the sample.

SEM (Jeol JCM-6000Plus) images of polished and fracture samples have been taken under mid-vacuum at 10Kv using a SE detector to observe and evaluate porosity and fracture surface of the samples. EDS was also performed at 15kv on polished samples and glass powder to detect any possible contamination in the sintering or polishing processes.

To resolve grain boundaries, additional micrographs were taken using FESEM (Zeiss Supra, Germany), which leverages the higher probe brightness/resolution of field-emission sources.

4.4 Electrochemical characterization

4.4.1 Electrochemical impedance spectroscopy

Electrochemical Impedance Spectroscopy (EIS) was used to evaluate the ionic conductivity of the glass–ceramic electrolytes by applying a small sinusoidal voltage to the sample and analyzing the current response over a wide frequency range. This approach enables the separation of contributions to ion transport originating from the bulk glass–ceramic phase and from interfaces, such as grain boundaries.

Samples were mounted in PAT-cells (EL-Cell GmbH, Germany) in Ar atmosphere inside a glovebox and measured using a Biologic potentiostat. Impedance spectra were recorded between −20 and 80 °C, with a frequency window ranging from 1 MHz to 0.1 Hz and an excitation amplitude of 10 mV. This interval was selected to capture both sub-ambient and moderately elevated conditions relevant for solid-state electrolytes applications.

Impedance spectra were fitted using EC-Lab software. The equivalent circuit depended on the regime:

- **High-temperature regime:** only capacitive branch intersecting the real impedance axis at R_1, where R_1 is the *combined* bulk + grain-boundary resistance; $R_{\text{tot}}=R_1$.

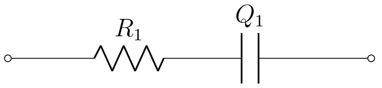

- **Medium-temperature regime:** partial semicircle at high frequency (HF), followed by a capacitive branch at low frequency (LF), where $R_1 + Q_1$ is in series with

$R_2 + Q_2$. R_1 (HF) corresponds to the bulk contribution, the related semicircle is not directly visible as it lies at frequencies higher than the instrumental limit; R_2 (LF) represents the grain boundary. The total resistance is $R_{\text{tot}} = R_1 + R_2$.

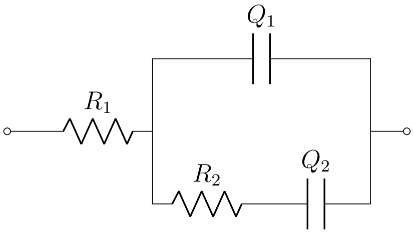

- **Low-temperature regime:** two depressed arcs plus low-frequency tail fitted with $Q_1 \,/\, (R_1{+}Q_2 \,/\, R_2{+}Q_3)$, accounting for bulk, grain boundaries, and electrode polarization.

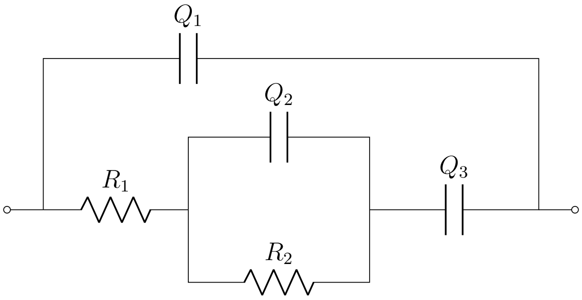

The ionic conductivity was computed as:

$$\sigma = \frac{t}{A \cdot R_{\text{tot}}} \tag{4.5}$$

where t is the pellet thickness and A the electrode surface area.

Electronic conductivity. In addition to ionic conductivity, the possible electronic contribution was also evaluated, being the material expected to have electronic conductivity close to the one of an insulator. After the impedance measurements, the same cells were subjected to a DC polarization test at 20°C in a symmetric blocking electrodes configuration. A constant voltage was applied using the Biologic potentiostat, and the resulting current was monitored over time until reaching a steady state. From the stabilized current, the electronic resistance R_{DC} was obtained, and the corresponding electronic conductivity calculated according to:

$$\sigma_e = \frac{t}{A \cdot R_{\text{DC}}} \tag{4.6}$$

4.4.2 Electrochemical stability window

The applicability of a solid electrolyte also depends on its electrochemical stability against Li metal and high-voltage cathodes. The electrochemical stability window (ESW) defines the potential range within which the electrolyte remains stable. Outside this window, decomposition and parasitic currents may occur.

Both the cathodic stability window (CSW) and the anodic stability window (ASW) were assessed by linear sweep voltammetry (LSV).

CSW Composite working electrodes were prepared by dispersing glass–ceramic powder (75 wt%), conductive carbon C65 (15 wt%), and PVDF (10 wt%) in NMP to form a homogeneous slurry. The slurry was cast on Cu foil, dried overnight at room temperature, then vacuum-dried at 120 °C for 24 h. 10 mm disks were punched and assembled in T cells inside an Ar-filled glovebox, with Li metal disks as counter and quasi-reference electrodes. Whatman GF/A separators (∼120 μm) were soaked in 1 m LiTFSI in PEO-G4 due to its known stability at low potentials vs. Li [26]. LSV was recorded at room T from OCV (ca 3V) to -0.2 V vs. Li at 0.1 mV s^{-1} using a (Biologic) electrochemical workstation.

ASW Oxidative stability was assessed in three electrodes Li//Au PAT cells. The gold working electrode (WE) was coated on one side of the pellet. A PEO-based polymer electrolyte containing 15% of LiTFSI (PEO–G4) was used as an interlayer to avoid direct ceramic/Li contact [26]. The reference Li metal ring was put in contact with the polymer electrolyte, allowing to carry out a three-electrodes measurement. LSV was run from OCV (ca 3V) to 6V vs. Li^+/Li at 0.1mVs^-1 using a (Biologic) electrochemical workstation.

In all cases the onset of sustained current increase was taken as the decomposition potential, defining the stability limit.

Chapter 5

Results and Discussion

In this chapter, the results obtained from the experimental campaign are presented. The focus is placed on the effect of $LiBO_2$ and $Li_2B_4O_7$ additions on the structural, microstructural, and electrochemical properties of LAMGP-based materials.

5.1 XRD Analysis of synthetized $Li_2B_4O_7$

The XRD analysis of the synthesized sample shown in Figure 5.1 confirms the successful formation of crystalline $Li_2B_4O_7$. The main reflections observed at approximately 21.7°, 25.5°, and 33–34.5° 2θ are in very good agreement with those reported in the ICDD reference card no. 01-079-0963 for tetragonal $Li_2B_4O_7$. This correspondence indicates that the synthesis route employed effectively stabilized the expected phase.

Importantly, no additional peaks corresponding to other lithium borates (such as $LiBO_2$, LiB_3O_5, or $Li_2B_8O_{13}$) were detected, confirming that the synthesized material consists predominantly of $Li_2B_4O_7$ within the detection limits of laboratory XRD.

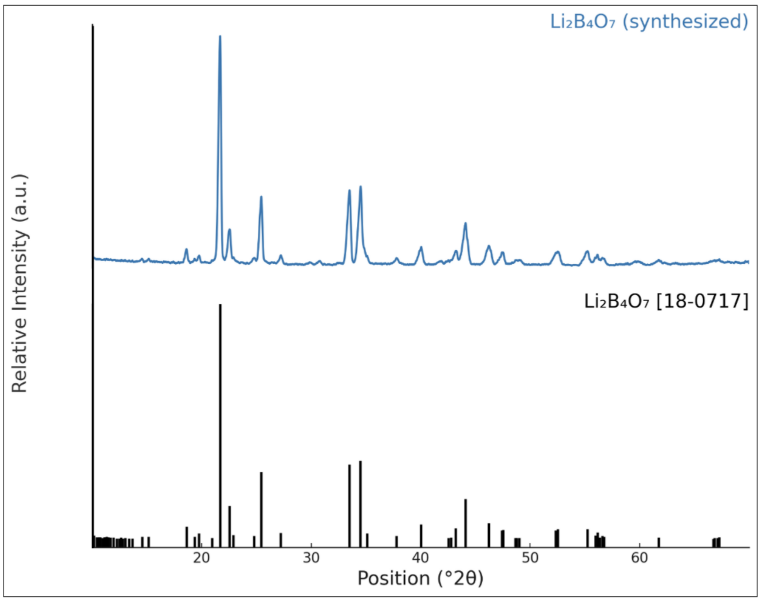

Figure 5.1: X-ray diffractogram of synthesized $Li_2B_4O_7$ (top) and from database (bottom).

5.2 LAMGP + $LiBO_2$/$Li_2B_4O_7$ characterization

5.2.1 Differential Scanning Calorimetry (DSC)

DSC showed similar results to those obtained by Saffirio et al. [27] for the samples containing $Li_2B_4O_7$. In this case, the T_g of the bulk glass is slightly higher than that of the glass powders, confirming a surface-driven crystallization mechanism typical of certain glass-ceramics [37]. In our case, the T_p values are essentially the same for both samples, indicating that crystallization occurs independently of surface effects. The characteristic temperatures are, however, significantly lower than those reported for LAMGP [27], suggesting that lithium tetraborate causes the sample to differ from the reference LAMGP samples.

The behavior of the samples containing $LiBO_2$ differs from that of the reference LAMGP samples [27]. There is a major difference in the T_p values between bulk glass and powders. In this case, $LiBO_2$ makes the crystallization phenomenon strongly surface-dependent, with a difference of about 40 °C between the two. There is also a larger difference between T_x and T_g, indicating that $LiBO_2$ provides higher glass stability to the NASICON network. The T_g values also show different behavior, with the bulk glass exhibiting a lower value than the powders.

The measurement results are shown in Figure 5.2, while the characteristic temperatures of the samples are listed in Table 5.1.

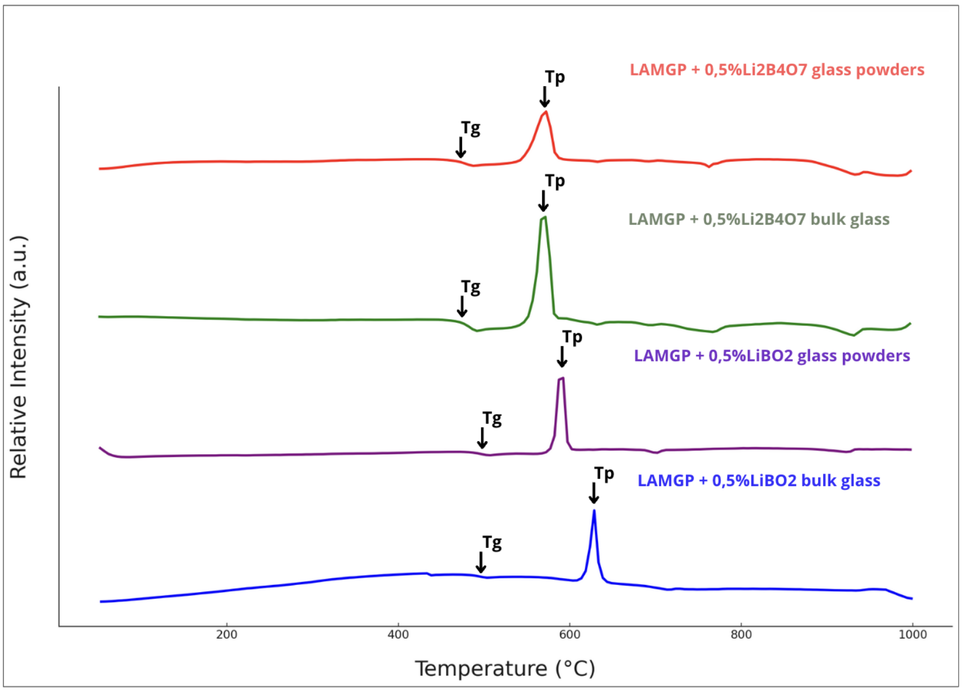

Figure 5.2: DSC of tested LAMGP bulk glasses and powders.

Table 5.1: Characteristic temperatures of the studied samples.

Sample	**T$_g$ (°C)**	**T$_p$ (°C)**
LAMGP + 0,5% $LiBO_2$ bulk glass	476.1	628.1
LAMGP + 0,5% $LiBO_2$ glass powders	477.7	589.8
LAMGP + 0,5% $Li_2B_4O_7$ bulk glass	473.0	568.9
LAMGP + 0,5% $Li_2B_4O_7$ glass powders	471.0	568.9

5.2.2 Hot Stage Microscopy (HSM)

HSM showed that the different compositions exhibited a shrinkage of 35.1% (LAMGP + $LiBO_2$) and 21% (LAMGP + $Li_2B_4O_7$), respectively. The first value falls between the shrinkage values reported for LAGP (38%) and LAMGPB (31%). B_2O_3 is likely a more effective sintering aid compared to the tested samples, although $LiBO_2$ still exert a significant effect on the material. The value related to $Li_2B_4O_7$ is significantly lower, indicating the ineffectiveness of this sintering aid in the material. From the HSM surface area vs. temperature curve shown in Figure 5.3, it can be observed that, above 800°C, the sample containing $LiBO_2$ starts to expand, presumably due to the lower melting temperature of the sintering aid, something that was not observed in the sample containing $Li_2B_4O_7$. This phenomenon suggests that the sintering aids maintained their original form and did not undergo major reactions with the NASICON structure. This can be further visualized in Figure 5.4, which shows images of the samples at their characteristic temperatures. The major difference is observable by comparing the samples at approximately 900°C.

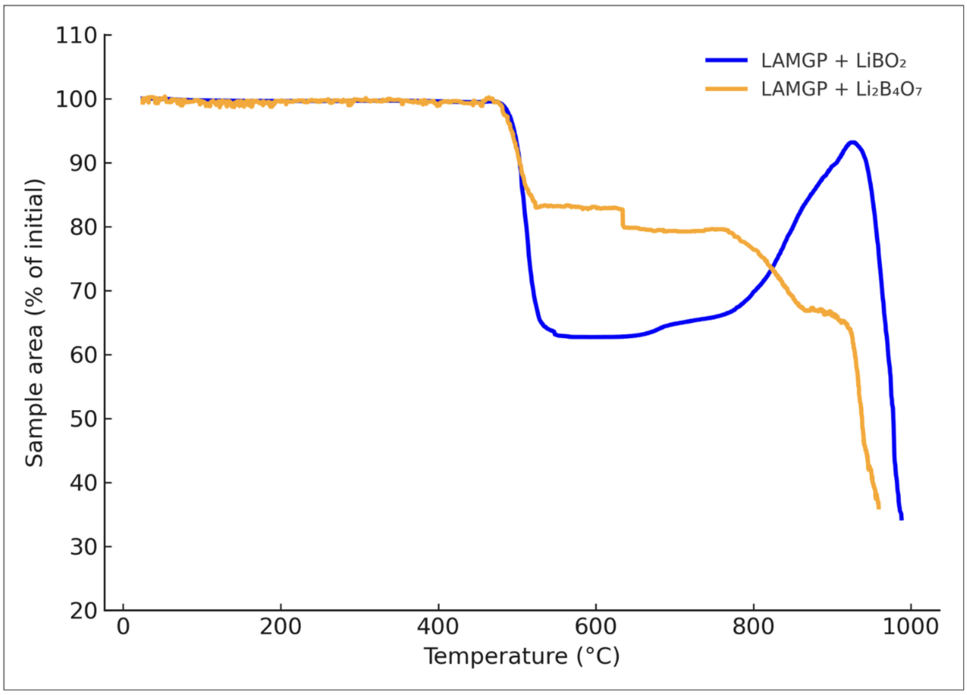

Figure 5.3: Sample area variation with temperature (acquired with HSM).

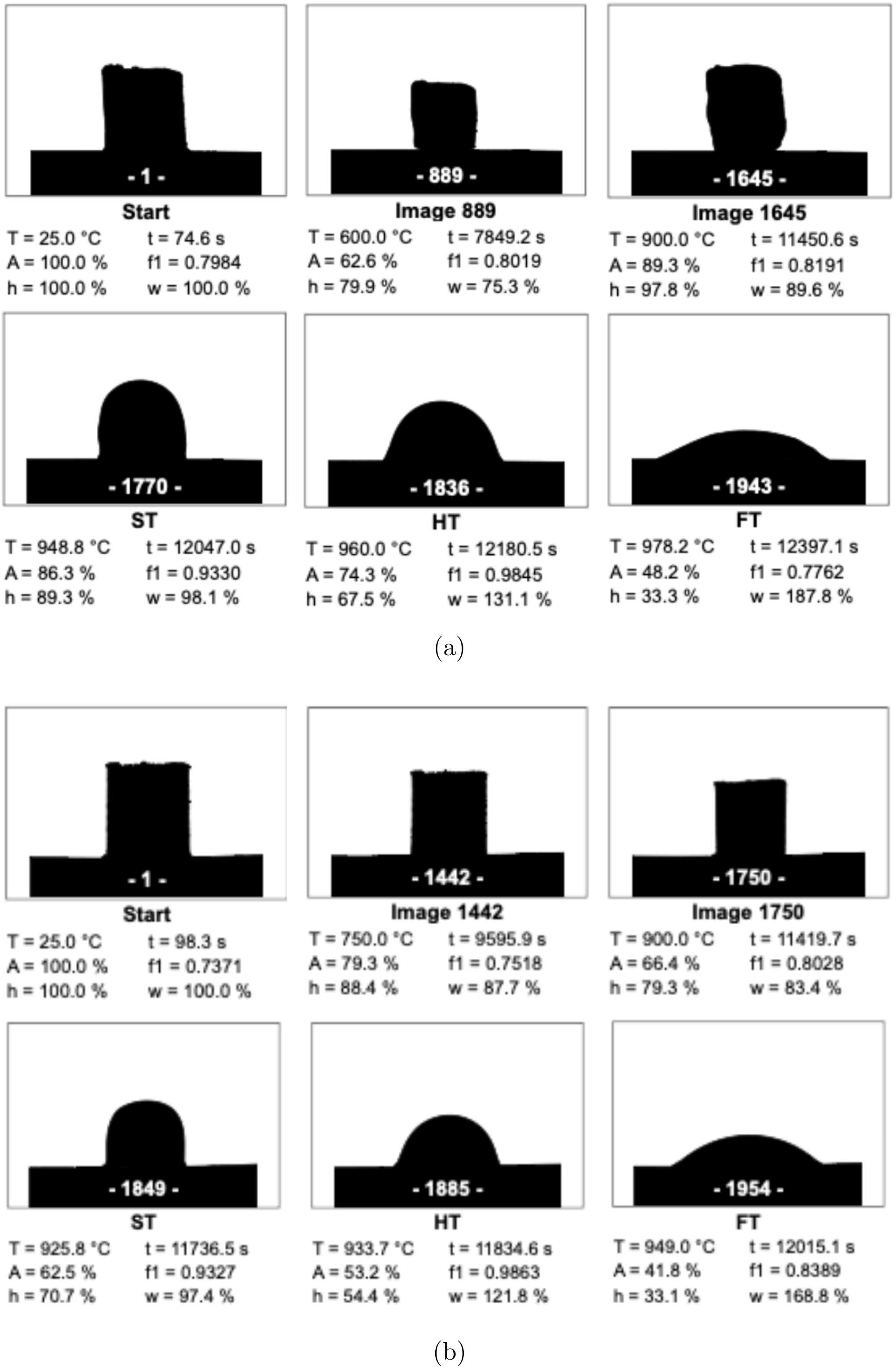

Figure 5.4: HSM images at different temperatures for LAMGP+$LiBO_2$ (a) and LAMGP+$Li_2B_4O_7$ (b).

5.2.3 Crystalline Phase Analysis

Phase identification was carried out by comparison with the $LiGe(PO_3)_4$ reference (ICDD card 01-080-1924), which displays an almost identical diffraction pattern with only minor shifts in peak positions due to the modification of the lattice parameters causes by the presence of magnesium. This approach has already been adopted in previous works on related LAMGP glass-ceramic systems [26, 27]. The XRD spectra for all LAMGP-based samples are shown in Figure 5.5, confronted with the reflections of the NASICON phase (indexed as $LiGe(PO_3)_4$). The reference pattern of GeO_2 is also displayed for direct comparison.

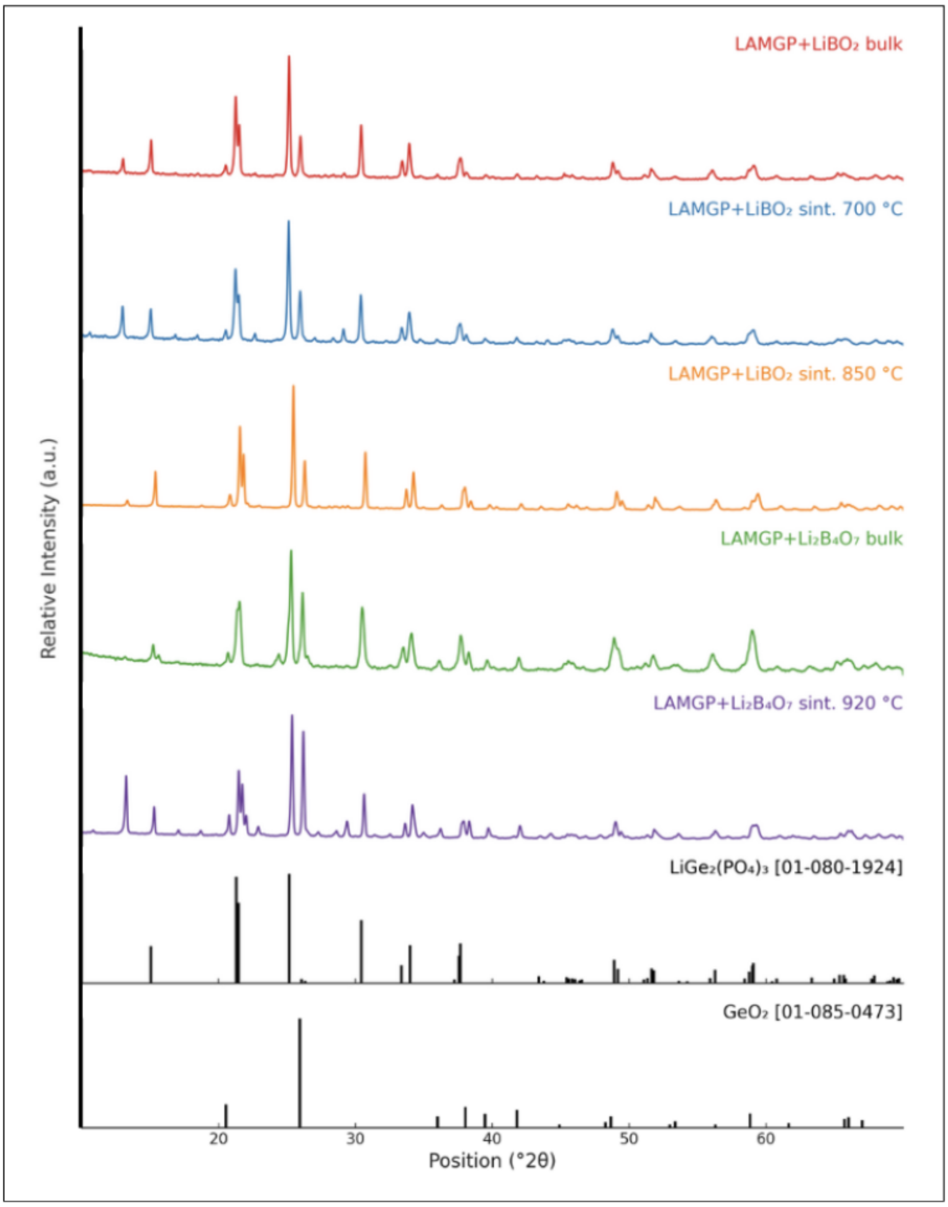

Figure 5.5: X-ray diffractoram of LAMGP containing 0,5 wt% $LiBO_2$ or $Li_2B_4O_7$, prepared whit different thermal treatments compared to $LiGe(PO_4)_3$ and GeO_2 from ICDD database.

In all analyzed samples, the presence of secondary germanium oxide (GeO_2, ICDD card 01-080-1924) was detected. This observation is consistent with reports on LAGP- and

LAGTP-based systems, where GeO_2 commonly appears as a secondary phase after prolonged thermal treatments due to Li volatilization. In the present case, its formation can be ascribed to extended sintering and crystallization. Despite the deliberate addition of excess Li_2CO_3 to the starting batch (3.75 wt%), the strategy was not fully effective in suppressing lithium loss, as GeO_2 reflections were systematically observed. Importantly, no reflections associated with $AlPO_4$ were identified, clarifying that aluminum remained fully incorporated into the NASICON lattice.

When comparing the various compositions and treatments, subtle differences become apparent. Upon sintering, GeO_2 peaks are consistently present, but their intensity increases significantly in the high-temperature samples (850 °C, 920 °C), confirming that lithium loss during thermal treatment becomes more pronounced at elevated temperatures.

Overall, the two borate-modified LAMGP systems exibit no substantial differences in terms of crystalline phases. Both are characterized by the NASICON structure, with GeO_2 serving as the primary secondary phase. The only noticeable exception is the pellet treated at 920 °C, which exhibits additional reflections attributable to minor secondary phases. These peaks were difficult to identify, but their presence confirms that lithium volatilization and phase segregation are more likely to occur at higher temperatures.

5.2.4 Density evaluation

The density values calculated through Archimedes' method, together with the relative values with respect to the theoretical density of LAGP. The values are reported in Table 5.2.

Table 5.2: Archimedes density values and relative densities (LAGP theoretical density: 3.42 g/cm^3) of LAMGP samples with $LiBO_2$ and $Li_2B_4O_7$ additives.

Sample	Density (g/cm^3)	Relative density (%)
LAMGP + $LiBO_2$ (bulk)	3.20	93.6
LAMGP + $LiBO_2$ (sintered 700 °C)	2.90	84.8
LAMGP + $LiBO_2$ (sintered 850 °C)	2.57	75.1
LAMGP + $Li_2B_4O_7$ (bulk)	3.18	93.0
LAMGP + $Li_2B_4O_7$ (sintered 700 °C)	2.96	86.6
LAMGP + $Li_2B_4O_7$ (sintered 920 °C)	2.82	82.5

The bulk samples, as expected, exhibit higher densities compared to the sintered ones, since sintering unavoidably leads do to the presence of residual sintering voids. The sintering temperature plays a significant role, as the sample sintered at 700 °C exhibits a relative density approximately 10% higher than that of the sample sintered at 850 °C. This behavior confirms the fact that lithium oxide tends to evaporate above a certain temperature, as already discussed in Section 5.2.2, in addition to a major release of gasses trapped during casting. The values obtained for the ceramic sintered at 920 °C are considered unreliable, because the tested sample shows macroporosity (few mm pores, visible on a large scale in Figure 4.7, sample 23) that allowed liquid infiltration, thus overestimating the density value. Minor differences are observed between ceramics containing $LiBO_2$ and $Li_2B_4O_7$ when sintered at the same temperature. Overall, the most effective method for densifying the material is through bulk glass crystallization, which enables a density of approximately 93% of the theoretical value to be achieved.

5.2.5 SEM imaging

Figure 5.6 shows the cross-section micrographs obtained through Scanning Electron Microscopy (SEM).

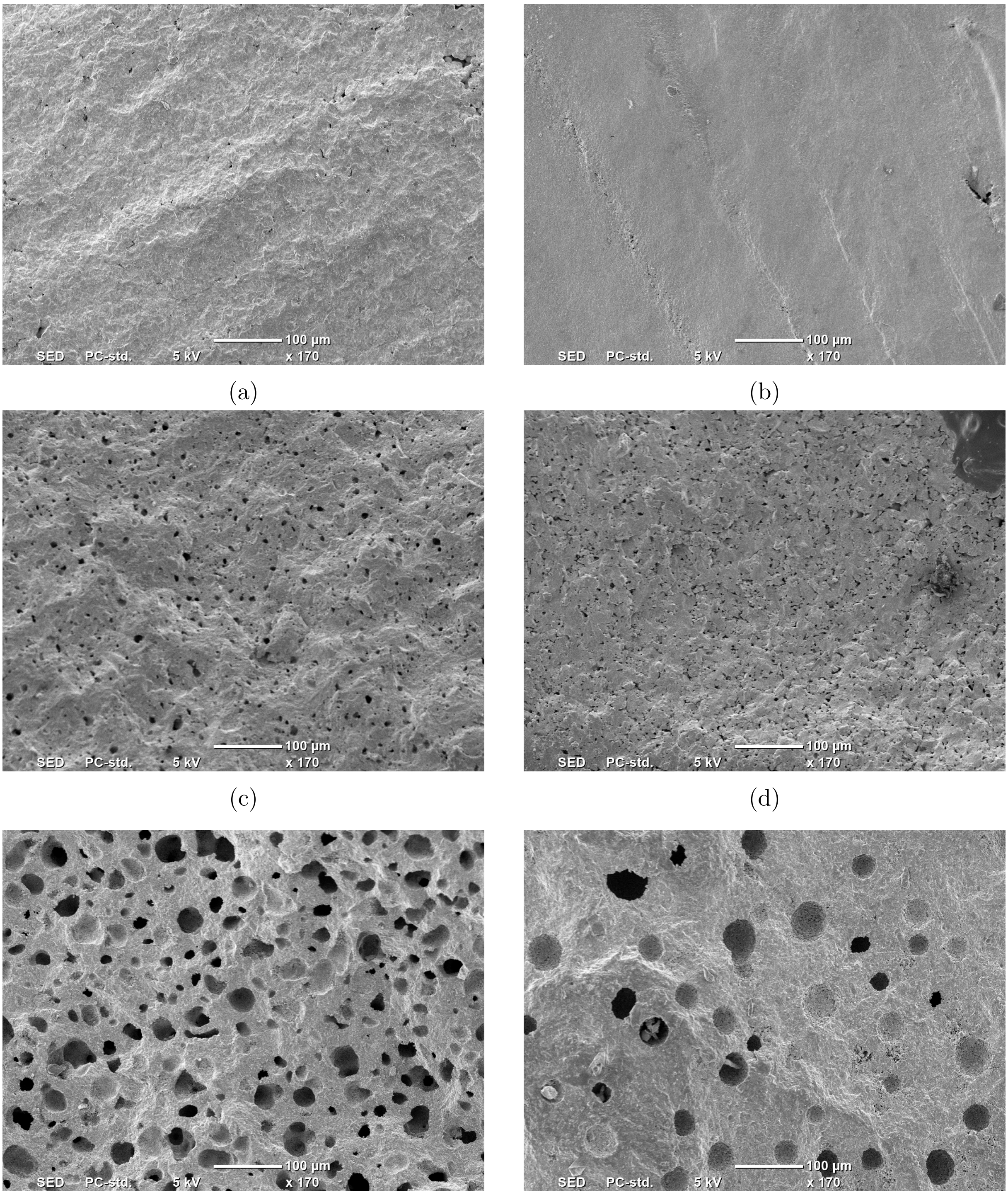

(a)

(b)

(c)

(d)

(e)

(f)

Figure 5.6: SEM images of different samples: a) LAMGP+$LiBO_2$ bulk, b)LAMGP+$Li_2B_4O_7$ bulk, c)LAMGP+$LiBO_2$ sintered 700°C, d)LAMGP+$Li_2B_4O_7$ sintered 700°C, e)LAMGP+$LiBO_2$ sintered 850°C, f)LAMGP+$Li_2B_4O_7$ sintered 920°C.

Bulk samples exhibit very less widespread voids, leading to limited porosity, in agreement with their higher measured densities. In contrast, samples sintered at 700 °C display a higher amount of pores, mostly in the form of microporosity. At higher sintering temperatures, the microstructure evolves towards macroporosity, which further explains the reduction in density values compared to the reference. The differences recorded between samples sintered at different temperatures can be attributed both to the release of trapped gasses during casting and to higher lithium oxide losses. No evident difference is observed between samples containing $LiBO_2$ and those containing $Li_2B_4O_7$.

Energy-dispersive X-ray spectroscopy (EDS) was performed both on the glass powders and on the sintered samples, as some of the latter showed grey spots on the surface suggesting possible contamination. The analysis confirmed this suspicion: in multiple samples, EDS detected a mild contamination (0.2–0.5 wt%) of calcium, which was not found in the glass powders. This contamination is likely ascribable to the polishing process, performed with streamline water instead of distilled water. However, considering that the contamination level is close to the detection limit of EDS, likely confined to the surface, and the absolute amount is negligible, it is not expected to significantly affect the properties of the samples.

5.2.6 Grain Boundary Imaging

The FESEM images acquired at 200 nm scale provide insights into the microstructural evolution of LAMGP samples with different additives and heat treatments. The bulk sample containing $LiBO_2$ (Fig. 5.7a) exhibits enhanced grain cohesion due to the presence of a glassy phase distributed at the grain boundaries. In this case, $LiBO_2$ appears to act as a transient liquid phase, improving intergranular contact.

In contrast, the bulk sample containing $Li_2B_4O_7$ (Fig. 5.7b) does not show a comparable improvement in grain cohesion, possibly because $Li_2B_4O_7$, having a higher melting temperature, does not form a transient liquid phase under the processing conditions, preventing the same liquid-assisted sintering mechanism from occurring.

While composition differences affect the structure of bulk samples, sintered samples seems unaffected, possibly because the sintering voids, despite the possible existence of liquid transient phases, are too large to be filled.

For the sintered samples with $LiBO_2$ (Fig. 5.7c), grain cohesion is not poor but it is clearly inferior to that of the bulk glass-crystallized sample. Sintering voids are still present and the liquid phase is not enough to fill all the gaps in the material.

Increasing the sintering temperature to 850 °C (Fig. 5.7e), leads to grain coarsening and morphological changes compared to the sample sintered at 700 °C, as expected, but no differences in grain cohesion. Nevertheless, the coarser microstructure obtained at higher temperature reduces the number of grain boundaries, lowering the resistance to Li^+ migration and, possibly, improving overall ionic conductivity despite the weak cohesion.

Sintered samples in Figures 5.7d and 5.7f exhibit a structure with very poor grain cohesion having both the problems related to sintering and the presence of $Li_2B_4O_7$.

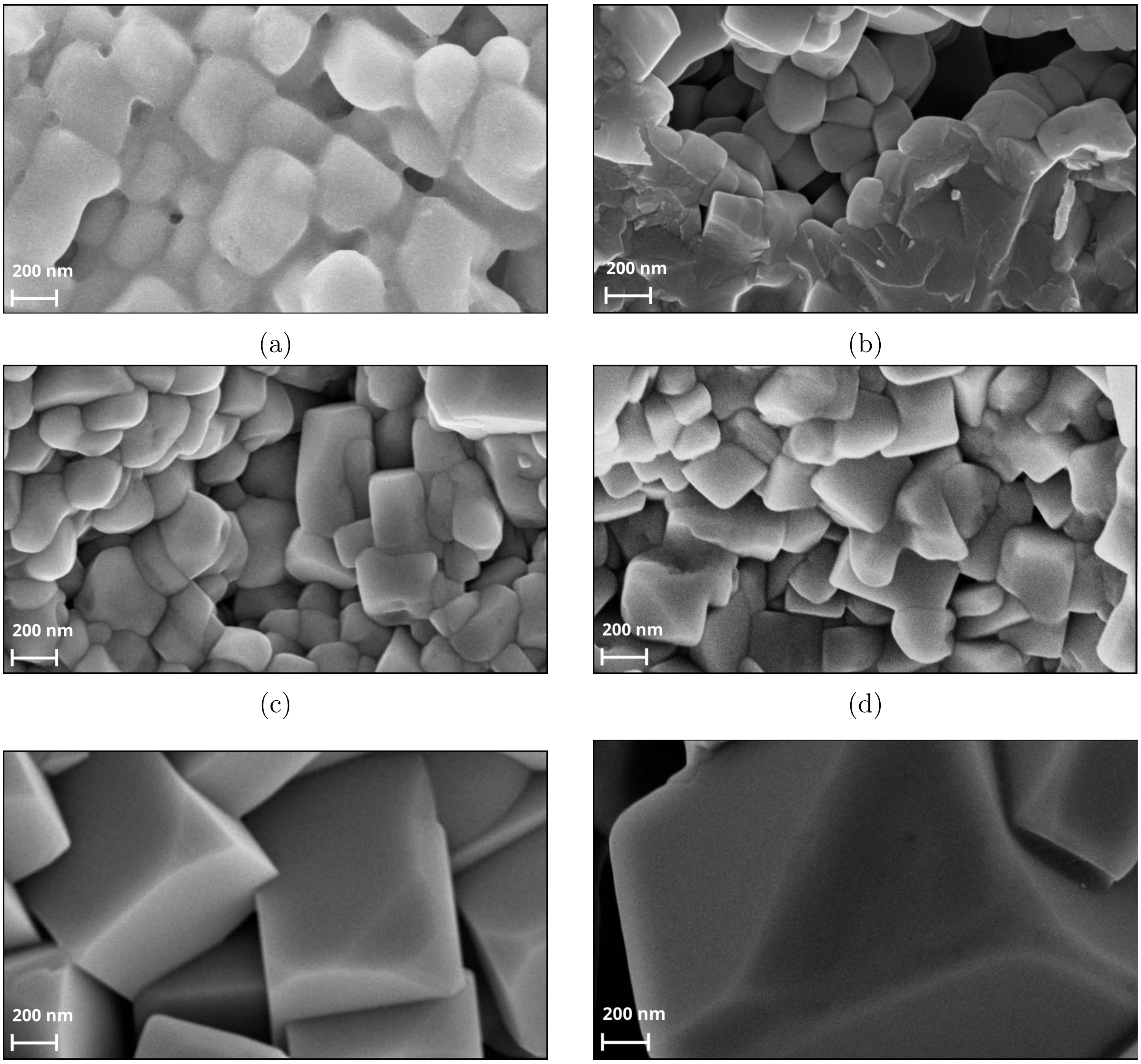

(a) (b) (c) (d) (e) (f)

Figure 5.7: Fesem micrographs of different samples: a) LAMGP+$LiBO_2$ bulk, b)LAMGP+$Li_2B_4O_7$ bulk, c)LAMGP+$LiBO_2$ sintered 700°C, d)LAMGP+$Li_2B_4O_7$ sintered 700°C e)LAMGP+$LiBO_2$ sintered 850°C, f)LAMGP+$Li_2B_4O_7$ sintered 920°C.

5.2.7 Electrochemical Impedance Spectroscopy (EIS)

Impedance spectra recorded at different temperatures were fitted using the equivalent circuits described in Section 4.4.1. As an example, Figure 5.8 reports impedance cycles, at different temperatures, of the bulk sample containing $LiBO_2$, each of which was fitted with a different equivalent circuit.

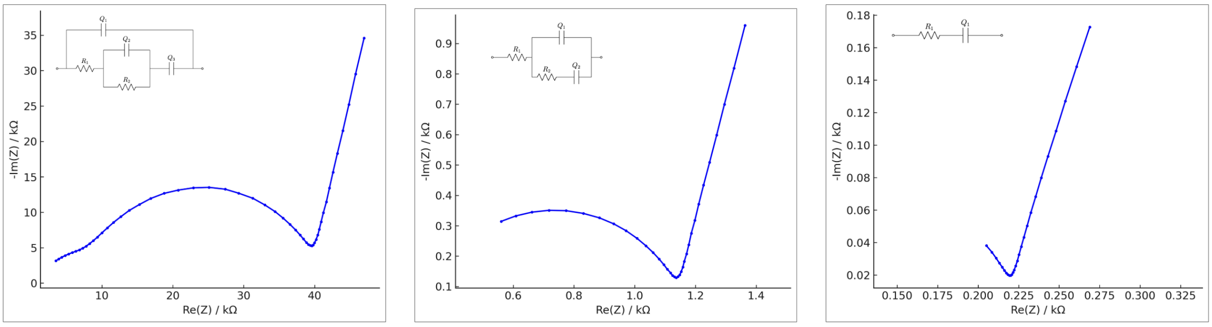

(a) (b) (c)

Figure 5.8: Representative Nyquist plots of the bulk sample containing $LiBO_2$, each fitted with a different equivalent circuit: a)EIS at -20°C, b)EIS at 40°C, EIS at 80°C.

Figure 5.9 shows the resistance values obtained through linear fitting of the impedance measurements as a function of temperature for LAMGP+$LiBO_2$ bulk sample, highlighting the different values of R_2 (grain boundary resistance) and R_1 (bulk resistance).

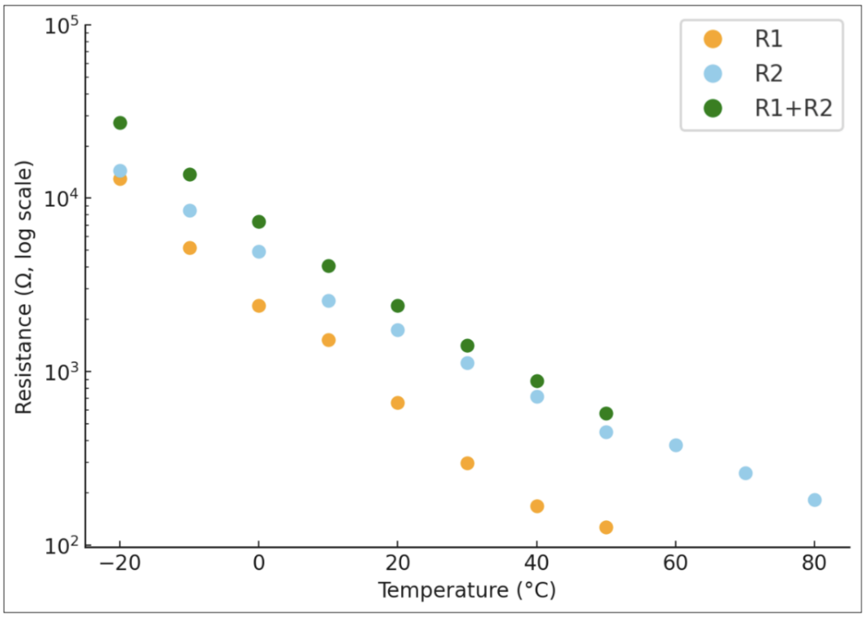

Figure 5.9: LAMGP + $LiBO_2$ (bulk processed) grain boundary (R_2) and bulk (R_1) resistance values at different temperatures.

The behavior is similar for all samples (reason for which only one is reported) but the values are not normalized for sample area or thickness and are therefore not intended for comparison between the different electrolytes. As expected, the grain boundary resistance (R_2) is consistently higher, with values at least three times greater than the bulk resistance (R_1), confirming that the grain boundaries are the main bottleneck for Li^+ ion transport.

Regarding the calculated ionic conductivity, the samples exhibited, as expected, two orders of magnitude difference between –20 °C and 80 °C. This variation is illustrated in Figure 5.10.

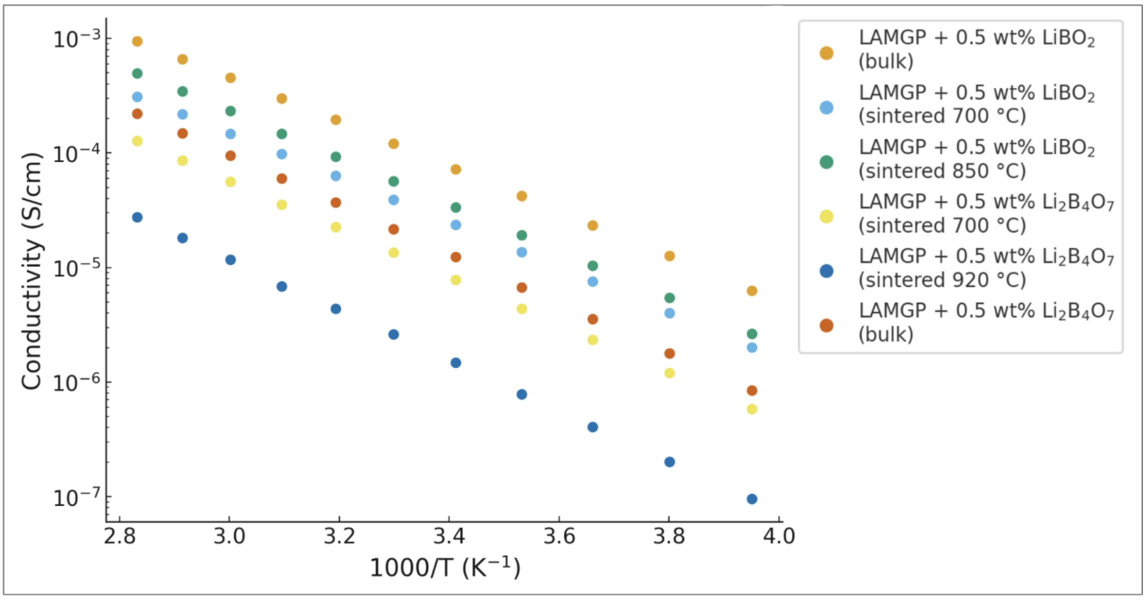

Figure 5.10: Temperature dependence of the total ionic conductivity of LAMGP-based samples with 0.5 wt% $LiBO_2$ or $Li_2B_4O_7$ in bulk and sintered forms.

When comparing the room-temperature values (20 °C) listed in Table 5.3, several trends can be highlighted:

- **Bulk $LiBO_2$** showed the highest conductivity, likely due to the excellent grain cohesion promoted by the formation of a transient liquid phase during processing.
- **All $Li_2B_4O_7$-containing samples** displayed very low conductivity compared to the other compositions. This might be ascribed to the absence of any observed liquid transient phase; indeed, $Li_2B_4O_7$ appears to have a detrimental effect, further reducing ionic conductivity. In particular, the sample sintered at 920 °C exhibited extremely low conductivity, which can likely be further increased by significant Li_2O volatilization, accompanied by secondary phases, at such high temperature.
- **$LiBO_2$-sintered samples** exhibited higher conductivity than all $Li_2B_4O_7$ samples, but lower than the bulk $LiBO_2$ specimen. This again indicates that grain cohesion was not significantly improved compared to the bulk due to the remaining sintering voids.
- **An interesting difference emerges between the $LiBO_2$ samples sintered at 700 °C and 850 °C**: the latter showed better conductivity. This effect is most likely attributable to the larger grain size at higher temperature, which reduces the number of grain boundaries that Li^+ ions must cross, thereby lowering the overall grain boundary resistance. It is unlikely that this improvement originates from the formation of a transient liquid phase, as no such feature was observed in the FESEM micrographs. The large porosity of the sample seems not to affect ionic conductivity or, if so, this effect is shaded by the positive ones.

Table 5.3: Total ionic conductivity at 20 °C for LAMGP samples containing 0.5 wt% $LiBO_2$ or $Li_2B_4O_7$.

Sample	σ **(S·cm^{-1}) at 20 °C**
LAMGP + $LiBO_2$ (bulk)	7.2×10^{-5}
LAMGP + $LiBO_2$ (sintered 700 °C)	2.4×10^{-5}
LAMGP + $LiBO_2$ (sintered 850 °C)	3.3×10^{-5}
LAMGP + $Li_2B_4O_7$ (bulk)	1.2×10^{-5}
LAMGP + $Li_2B_4O_7$ (sintered 700 °C)	7.8×10^{-6}
LAMGP + $Li_2B_4O_7$ (sintered 920 °C)	1.5×10^{-6}

In the present work, the best composition (LAMGP+$LiBO_2$ bulk) displayed conductivities below 1×10^{-4} S/cm at 20 °C, whereas Saffirio and co-workers reported values as high as 2×10^{-4} S/cm for LAMGP + B_2O_3 [27]. This comparison indicates that, while $LiBO_2$ provides a measurable improvement compared to undoped samples, B_2O_3 is a more efficient additive to enhance ionic conductivity in phosphate-based NASICON electrolytes.

5.2.8 Electronic conductivity

All samples exhibited electronic conductivity values (listed in Table 5.4) sufficiently low to be considered suitable for use as solid electrolytes.

Table 5.4: Electronic conductivity.

Sample	σ_e (S cm^{-1})
LAMGP+$LiBO_2$ (bulk)	1.94×10^{-9}
LAMGP+$LiBO_2$ (sintered 700 °C)	1.12×10^{-9}
LAMGP+$LiBO_2$ (sintered 850 °C)	7.58×10^{-10}
LAMGP+$Li_2B_4O_7$ (bulk)	1.24×10^{-9}
LAMGP+$Li_2B_4O_7$ (sintered 700 °C)	2.56×10^{-10}
LAMGP+$Li_2B_4O_7$ (sintered 920 °C)	2.68×10^{-9}

5.2.9 Electrochemical Stability Window (ESW)

The anodic stability window (ASW) of the electrolyte was evaluated from the current–voltage (I–V) curves shown in Figure 5.11. For all samples, the curves display an initial increase in current, corresponding to the point where the signal deviates from zero and marking the onset of electrochemical reactions. This stage is subsequently followed by an exponential increase in current, which defines the final limit of stability.

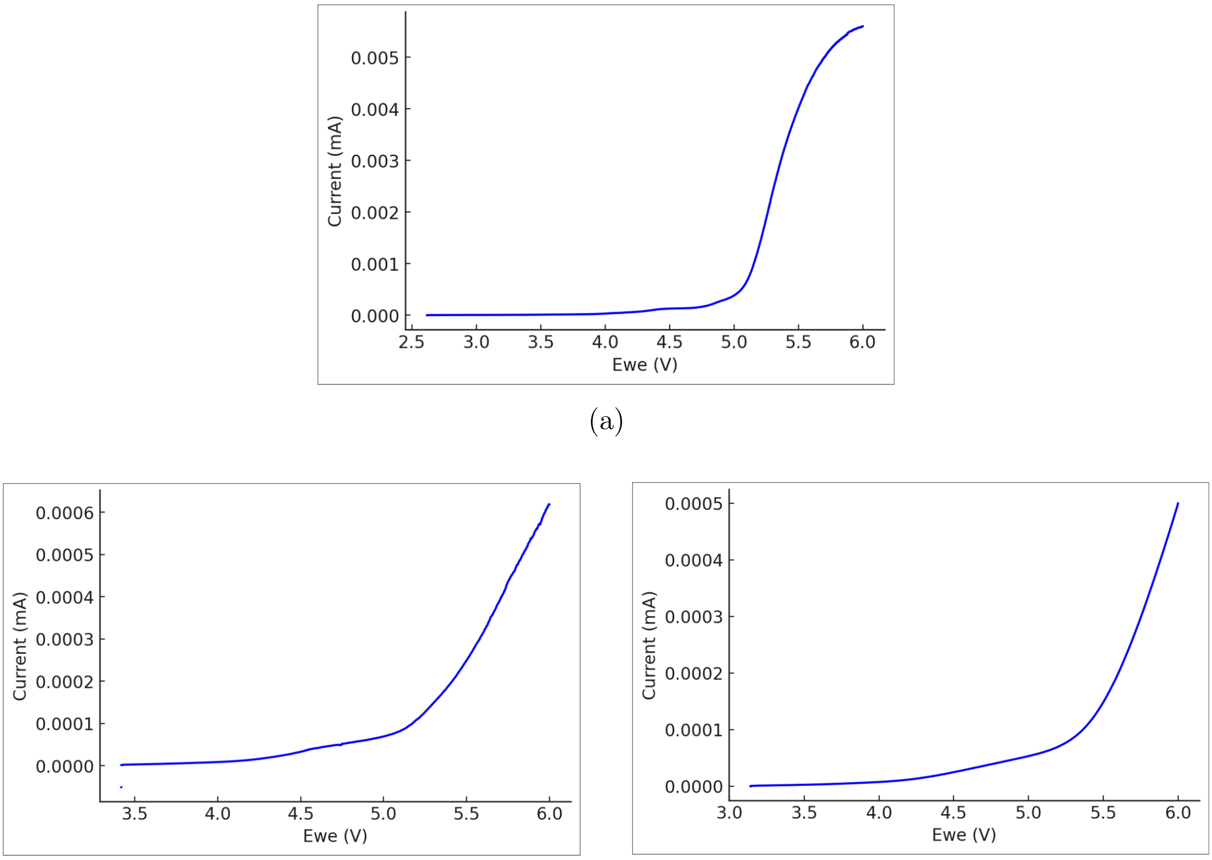

(a)

(b) (c)

Figure 5.11: LSV from OCV to 6V for LAMGP+$LiBO_2$ bulk (a), LAMGP+$LiBO_2$ sintered at 700°C (b) and LAMGP+$Li_2B_4O_7$ sintered at 700°C.

The values of the onset oxidation and the exponential increase are reported in Table 5.5. All three tested samples exhibited an onset of oxidation between 4.00 and 4.15 V, while the final oxidation voltage ranged from 4.75 to 5.25 V.

Table 5.5: Anodic stability window (ASW) values determined by linear sweep voltammetry.

Sample	First oxidation onset [V]	Exponential increase [V]
LAMGP+$LiBO_2$ (bulk)	4.00	4.75
LAMGP+$LiBO_2$ (sintered 700 °C)	4.15	5.15
LAMGP+$Li_2B_4O_7$ (sintered 700 °C)	4.15	5.25

The cathodic stability window (CSW) of the electrolyte was evaluated from the current–voltage (I–V) curves shown in Figure 5.12. For all samples, the curves exhibit an initial decrease in current corresponding to the point of onset of the reduction processes. This stage is subsequently at lower voltages followed by more pronounced decreases in current and/or by the final drop which define the effective limit of cathodic stability due to the red-ox activity of Germanium.

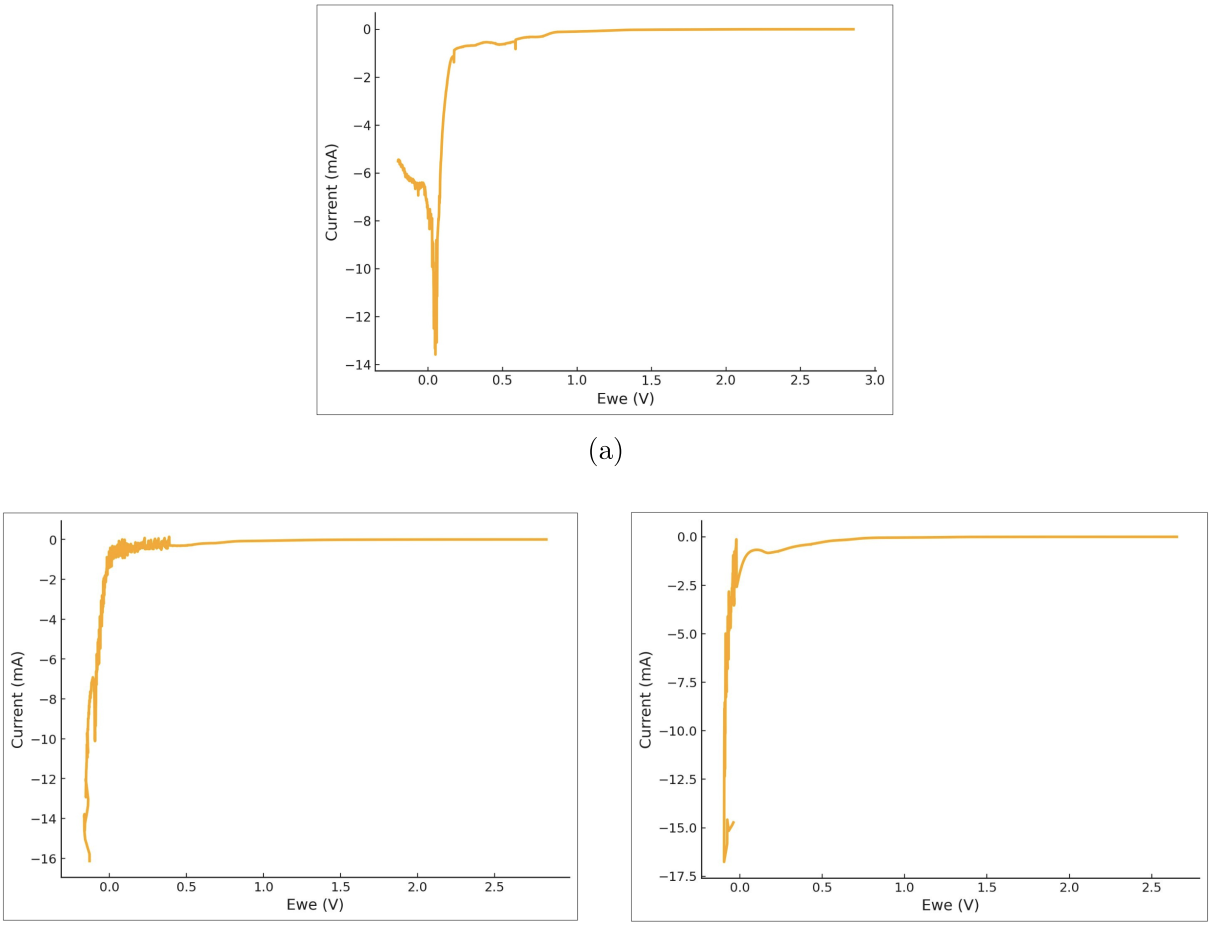

(a)

(b) (c)

Figure 5.12: Linear sweep voltammetry of the cathodic branch (OCV from -0.2V vs. Li) for LAMGP+$LiBO_2$ bulk (a), LAMGP+$LiBO_2$ sintered at 700°C (b) and LAMGP+$Li_2B_4O_7$ sintered at 700°C (c).

The values of the cathodic drops are reported in Table 5.6. As in the anodic case, the sintered samples containing $LiBO_2$ exhibit slightly higher stability compared to the bulk ones. The main drop in cathodic stability was observed between 0.50 and 0.15V. Interestingly, the sample containing $Li_2B_4O_7$ displayed two distinct steps followed by a temporary stabilization, instead of a single drop as observed in the other samples. Moreover, in this sample, the current values below 0.5 V showed large fluctuations, indicating a higher degree of instability, confirmed by the very early first step at around 1.3V.

Table 5.6: Cathodic stability window (CSW) values determined by cyclic voltammetry. The first, second, and third drops denote successive reduction processes observed.

Sample	First drop [V]	Final drop [V]
LAMGP + $LiBO_2$ (bulk)	0.85	0.15
LAMGP + $LiBO_2$ (sintered 700 °C)	0.80	0.05
LAMGP + $Li_2B_4O_7$ (sintered 700 °C)	1.30	0.10

Chapter 6

Conclusions

In the followings, the main findings of the present experimental master's Thesis work are summarized. The conclusions are drawn regarding the effect of $LiBO_2$ and $Li_2B_4O_7$ additions on the thermal behavior, crystalline phase evolution, microstructure, and electrochemical performance of LAMGP-based glass-ceramics. Future research perspectives are also briefly outlined.

6.1 Results summary

The main aim of this Master's Degree Thesis was investigating the influence of borate modifiers on the $Li_{1.5}Al_{0.3}Mg_{0.1}Ge_{1.6}(PO_4)_3$ (LAMGP), a promising NASICON-type glass-ceramic electrolyte material for solid-state battery applications. Based on previous results demonstrating that the addition of B_2O_3 significantly improved the properties of this system, the work focused on an experimental study of LAMGP glass-ceramics modified with $LiBO_2$ and $Li_2B_4O_7$, trying at identifying how borate additives can be exploited to optimize NASICON-type electrolytes. A thorough analysis of how these additives influence the crystallization behavior, microstructure, and electrochemical properties was performed.

Thermal analysis revealed that $LiBO_2$ increases the glass stability and enhances the surface sensitivity of crystallization. In contrast, $Li_2B_4O_7$ exerted little influence on the onset of crystallization and did not significantly support densification during thermal treatment. These differences were confirmed by hot stage microscopy, where $LiBO_2$ exhibited a modest shrinkage effect, whereas $Li_2B_4O_7$ induced barely measurable densification.

XRD demonstrated that all compositions crystallize predominantly into the NASICON-type framework, with GeO_2 consistently present as a secondary phase due to lithium volatilization. At higher processing temperatures the extent of secondary phases increased, particularly for $Li_2B_4O_7$, which is consistent with its poor ability to stabilize the lithium-containing network during sintering.

The microstructural investigation corroborated these findings. $LiBO_2$ led to denser morphologies and improved grain cohesion, likely due to the transient formation of a liquid phase that assists sintering. In contrast, $Li_2B_4O_7$ produced poorly interconnected grains, indicatin its inability to contribute to liquid-phase-assisted densification.

These structural differences were directly mirrored in the electrochemical performance. The best ionic conductivity was achieved for bulk-crystallized $LiBO_2$ samples, which reached about 7×10^{-5} S cm^{-1} at room temperature, while sintered specimens showed slightly lower values in the 10^{-5} S cm^{-1} range. Conversely, $Li_2B_4O_7$-modified materials performed very poorly, with conductivities as low as 10^{-6} S cm^{-1}, confirming its detrimental effect on lithium mobility.

When set against the state of the art, the gap with the benchmark identified by Saffirio and co-workers (2024) [27] becomes clear. Their study on B_2O_3-modified LAMGP achieved room-temperature conductivities on the order of 2×10^{-4} S cm^{-1}, values substantially higher than those obtained here with $LiBO_2$ and $Li_2B_4O_7$. This comparison underscores that, among borate additives, B_2O_3 remains the most effective promoter of densification and ionic transport.

One of the most interesting results of this study was the beneficial effect of higher-temperature sintering. Samples treated at 850 °C showed improved microstructure and conductivity compared to those processed at 700 °C, suggesting that optimized high-temperature protocols can enhance the overall performance of LAMGP-based electrolytes.

6.2 Future Prospects

The positive effect of the increased sintering temperature opens the way for future investigations where the most effective sintering aid identified in the literature, B_2O_3, could be combined with such optimized schedules. Exploring the synergy between B_2O_3 additions and higher-temperature sintering may lead to materials that outperform the current state-of-the-art.

Additionally, the versatility of the LAMGP structure makes it a promising candidate for hybrid electrolytes, where ceramic phases are dispersed in polymer matrices. Owing to its aliovalent composition and the higher concentration of lithium vacancies compared to standard LAGP or LATP, LAMGP may provide superior ion transport in composite systems, a direction that remains largely unexplored.

The continued development of these electrolytes is also crucial from an application perspective. For lithium-based solid-state batteries, enabling the safe use of lithium-metal anodes is one of the most effective strategies to drastically increase energy density. Similarly, in the sodium system, the deployment of sodium-metal anodes essentially requires the use of solid electrolytes, as liquid electrolytes cannot provide sufficient protection against dendrite growth and interfacial instability. Advancing the understanding and optimization of NASICON-type materials, both as a glass–ceramic and as a component of hybrid electrolytes, therefore represents a strategic step toward high-energy solid-state batteries in both lithium and sodium chemistries.

List of Acronyms and Symbols

Acronyms

ASW	Anodic Stability Window
AU	Arbitrary Units
CSW	Cathodic Stability Window
LSV	Linear Sweep Voltammetry
DSC	Differential Scanning Calorimetry
EIS	Electrochemical Impedance Spectroscopy
ESW	Electrochemical Stability Window
FESEM	Field Emission Scanning Electron Microscopy
FSI	Bis(fluorosulfonyl)imide
HF	High Frequency
HSM	Hot Stage Microscopy
ICDD	International Centre of Diffraction Data
LAMGP	Lithium Aluminium Magnesium Germanium Phosphate
LF	Low Frequency
LFP	Lithium Iron Phosphate
LLTO	Lithium Lanthanum Titanate
LLZO	Lithium Lanthanum Zirconium Oxide
NASICON	Sodium Super Ionic Conductor
NMP	N-Methyl-2-pyrrolidone
OCV	Open Circuit Voltage
PAN	Poly(acrylonitrile)
PC	Poly(carbonate)
PEO	Poly(ethylene oxide)
PMMA	Poly(methyl methacrylate)
PVDF	Poly(vinylidene fluoride)
SE	Secondary Electrons
SEM	Scanning Electron Microscopy
SSB	Solid State Batteries
TFSI	Bis(trifluoromethanesulfonyl)imide
XRD	X-Ray Diffraction

Symbols

T_g	Glass transition temperature
T_x	Onset crystallization temperature
T_p	Peak crystallization temperature
ρ	Density
σ_i	Ionic conductivity
E_a	Activation energy
σ_e	Electronic conductivity

Bibliography

[1] J.-M. Tarascon and M. Armand, "Issues and challenges facing rechargeable lithium batteries," *Nature*, vol. 414, pp. 359–367, 2001.

[2] C. Gerbaldi, *Mesoporous Materials and Nanostructured LiFePO$_4$ as cathodes for Secondary Li-Ion Batteries: synthesis and characterization.* PhD thesis, Politecnico di Torino, 2006.

[3] K. Taehoon, Q. Yabing, S. Wentao, S. Dae-Yong, and O. Luis K., "Lithium-ion batteries: outlook on present, future, and hybridized technologies," *Journal of Materials Chemistry A*, vol. 7, p. 2942–2964, 2019.

[4] Y. Liu, Q. Liu, L. Xin, Y. Liu, F. Yang, E. A. Stach, and J. Xie, "Making li-metal electrodes rechargeable by controlling the dendrite growth direction," *Nature Energy*, vol. 2, 2017.

[5] L. Byeongyong, P. Eunsu, M. David, and W. L. Seung, "Sodium metal anodes: Emerging solutions to dendrite growth," *Chemical Reviews*, vol. 119, pp. 5416–5460, 2019.

[6] Z. Jian, Y.-S. Hu, X. Ji, and W. Chen, "Nasicon-structured materials for energy storage," *Advanced Materials*, vol. 29, 2017.

[7] K. Philippe, "Inorganic solid li ion conductors: An overview," *Solid State Ionics*, vol. 180, p. 911–916, 2009.

[8] F. Theodosios, C. Pieremanuele, D. James A., I. M. Saiful, and M. Christian, "Fundamentals of inorganic solid-state electrolytes for batteries," *Nature Materials*, vol. 18, p. 1278–1291, 2019.

[9] F. Lei, W. Shuya, L. Siyuan, L. Qi, and L. Yingying, "Recent progress of the solid-state electrolytes for high-energy metal-based batteries," *Advanced Energy Materials*, vol. 8, 2018.

[10] S. Chunwen, L. Jin, G. Yudong, W. David P., and Z. Jiujun, "Recent advances in all-solid-state rechargeable lithium batteries," *Nano Energy*, vol. 33, p. 363–386, 2017.

[11] A. M. Stephan, "Review on gel polymer electrolytes for lithium batteries," *European Polymer Journal*, vol. 42, 2006.

[12] K. Takada, "Progress and prospective of solid-state lithium batteries," *Acta mineraria*, vol. 62, pp. 759–770, 2013.

[13] Z. Xue, D. He, and X. Xie, "Poly(ethylene oxide)-based electrolytes for lithium-ion batteries," *Journal of Materials Chemistry A*, vol. 3, pp. 19218–19253, 2015.

[14] J. Janek and W. G. Zeier, "A solid future for battery development," *Nature Energy*, vol. 1, 2016.

[15] N. Anantharamulu, R. Koteswara Rao, G. Rambabu, B. Vijaya Kumar, V. Radha, and M. Vithal, "A wide-ranging rewiew on nasicon type materials," *Journal of Material Science*, vol. 46, pp. 2821–2837, 2011.

[16] W. Zhou, Y. Li, S. Xin, and J. B. Goodenough, "Rechargeable sodium all-solid-state battery," *ACS Central Science*, vol. 3, pp. 52–57, 2017.

[17] J. W. Fergus, "Ceramic and polymeric solid electrolytes for lithium-ion batteries," *Journal of Power Sources*, vol. 195, pp. 4554–4569, 2010.

[18] A. Sazvar, S. Ghahramani, O. Banapour Ghaffari, S. A. Zargar, and M. Golmohammad, "Review of advances and challenges in $Li_7La_3Zr_2O_{12}$ solid electrolytes: From processing to performance," *Journal of Power Sources*, vol. 657, 2025.

[19] J. Awaka, A. Takashima, K. Kataoka, N. Kijima, Y. Idemoto, and J. Akimoto, "Crystal structure of fast lithium-ion-conducting cubic $Li_2La_3Zr_2O_{12}$," *Chemistry Letters*, vol. 40, pp. 60–62, 2011.

[20] Z. Jiang, Y. Lou, Z. Fu, H. Ruan, and Y. Long, "Influence of particle size distribution on the microstructure, density and ionic conductivity of $Li_{6.25}Ga_{0.25}La_3Zr_2O_{12}$ ceramics," *Ceramics International*, vol. 51, pp. 38712–38722, 2025.

[21] A. Gruendl, S. Weinmann, J. Goehmann, J. Landau, M. Lechner, L. Mueller, K. J. Kim, J. L. M. Rupp, and M. F. Zaeh, "Process strategies for the laser-based surface treatment of garnet-type ceramics used in solid-state batteries," *Optics and Laser Technology*, vol. 189, 2025.

[22] M. Weiss, D. A. Weber, S. Anatoliy, J. Jurgen, and Z. Wolfang G., "Correlating transport and structural properties in $Li_{1+x}Al_xGe_{2-x}(PO_4)_3$ (LAGP) prepared from acqueous solution," *ACS Applied Materials & Interfaces*, vol. 10, pp. 10935–10942, 2018.

[23] M. Guin and F. Tietz, "Survey of the transport properties of sodium superionic conductor materials for use in sodium batteries," *Journal of Power Sources*, vol. 273, pp. 1056–1064, 2015.

[24] G. J. Kim, Y. H. Kim, S. K. Choi, J. W. Bae, K.-J. Lee, and M. Yang, "Effect of bimodal particle size distribution on $Li_{1.5}Al_{0.5}Ti_{1.5}(PO_4)_3$ solid electrolytes: Microstructures and electrochemical properties," *Powder Technology*, vol. 466, 2025.

[25] H. Bai, J. Hu, X. Li, Y. Duan, F. Shao, T. Kozawa, M. Naito, and J. Zhang, "Influence of $libo_2$ addition on the microstructure and lithium-ion conductivity of $Li_{1+x}Al_xTi_{2x}(PO_4)_3$ (x = 0.3) ceramic electrolyte," *Ceramics International*, vol. 44, no. 5, pp. 6558–6563, 2018.

[26] S. Saffirio, M. Falco, G. B. Appetecchi, F. Smeacetto, and C. Gerbaldi, "$Li_{1.4}Al_{0.4}Ge_{0.4}Ti_{1.4}(PO_4)_3$ promising NASICON-structured glass-ceramic electrolyte for all-solid-state li-based batteries: Unravelling the effect of diboron trioxide," *Journal of the European Ceramic Society*, vol. 42, no. 3, pp. 1023–1032, 2022.

[27] S. Saffirio, H. Darjazi, M. E. C. Pascuzzi, F. Smeacetto, and C. Gerbaldi, "Melt-casted $Li_{1.5}Al_{0.3}Mg_{0.1}Ge_{1.6}(PO_4)_3$ glass ceramic electrolytes: A comparative study on the effect of different oxide doping," *Heliyon*, vol. 10, no. 2, 2024.

[28] A. V. Kirianova, I. I. Yakovlev, D. S. Zimbovskii, S. Xiong, D. P. Sadykov, L. G. Grigoryan, X. Xu, D. Zhou, D. I. Yakubovsky, P. V. Evdokimov, I. A. Veselova, A. V. Arsenin, V. S. Volkov, F. S. Napolskiy, A. V. Merkulov, A. A. Rudnyh, V. A. Krivchenko, and O. O. Kapitanova, "Design of composite gel-polymer electrolytes with nanosized solid-state electrolyte particles for high power lithium-ion batteries," *Journal of Energy Storage*, vol. 132, 2025.

[29] Y. Yu, J. Zhu, J. Zhang, and M. Jiang, "Single-ion conducting polyoxadiazole-$Li_{1.3}Al_{0.3}Ti_{1.7}(PO_4)_3$ composite electrolytes: A robust quasi-solid polymer electrolyte enabling safe and durable lithium metal batteries," *Journal of Power Sources*, vol. 655, 2025.

[30] K. He, Y. Wang, C. Zu, H. Zhao, Y. Liu, J. Chen, B. Han, and J. Ma, "Influence of Al_2O_3 additions on crystallization mechanism and conductivity of Li_2O–Ge_2O–P_2O_5 glass–ceramics," *Physica B*, vol. 406, pp. 3947–3950, 2011.

[31] H. S. Jadhav, M.-S. Cho, R. S. Kalubarme, J.-S. Lee, K.-N. Jung, K.-H. Shin, and C.-J. Park, "Influence of B_2O_3 addition on the ionic conductivity of $Li_{1.5}Al_{0.5}Ge_{1.5}(PO_4)_3$ glass ceramics," *Journal of Power Sources*, vol. 241, pp. 502–508, 2013.

[32] A. Curcio, A. G. Sabato, M. Nuñez Eroles, J. C. Gonzalez-Rosillo, A. Morata, A. Tarancón, and F. Ciucci, "Ultrafast crystallization and sintering of $Li_{1.5}Al_{0.5}Ge_{1.5}(PO_4)_3$ glass and its impact on ion conduction," *ACS Applied Energy Materials*, vol. 5, no. 11, p. 14466–14475, 2022.

[33] D. Zhou, X. Xu, S. Xiong, A. V. Garshev, I. A. Veselova, V. I. Putlayev, P. V. Evdokimov, and O. O. Kapitanova, "Glass-ceramic two-phase sintering enhancing electro-chemo-mechanical properties of NASICON electrolyte for solid-state batteries," *Chemical Engineering Journal*, vol. 520, 2025.

[34] S. Saffirio, A. G. Sabato, D. M. Ferreira, A. Tarancón, C. Gerbaldi, and F. Smeacetto, "Enhanced densification and conductivity of LAMGPB glass-ceramic electrolyte through ultra-fast high-temperature sintering," *Journal of Power Sources*, vol. 640, 2025.

[35] L. Brewer and J. Margrave, "The vapor pressures of lithium and sodium oxides," *The Journal of Physical Chemistry*, vol. 59, no. 5, pp. 421–428, 1955.

[36] E. Pekpak, A. Yılmaz, and G. Özbayoğlu, "The effect of synthesis and doping procedures on thermoluminescent response of lithium tetraborate," *Journal of Alloys and Compounds*, vol. 509, no. 5, pp. 2466–2472, 2011.

[37] A. G. Sabato, M. Salvo, A. De Miranda, and F. Smeacetto, "Crystallization behaviour of glass-ceramic sealant for solid oxide fuel cells," *Materials Letters*, vol. 141, pp. 284–287, 2015.

List of Figures

List of Tables